Estimation of Variance and Spatial Correlation Width for Fine-Scale Measurement Error in Digital Elevation Model

Mikhail Uss, Benoit Vozel, Vladimir Lukin, Kacem Chehdi

Estimation of Variance and Spatial Correlation Width for Fine-Scale Measurement Error in Digital Elevation Model

Mikhail L. Uss, Benoit Vozel, Vladimir V. Lukin, and Kacem Chehdi

***Abstract*— In this article, we borrow from the blind noise parameter estimation (BNPE) methodology early developed in the image processing field an original and innovative no-reference approach to estimate digital elevation model (DEM) vertical error parameters without resorting to a reference DEM. The challenges associated with the proposed approach related to the physical nature of the error and its multifactor structure in DEM are discussed in detail. A suitable multivariate method is then developed for estimating the error in gridded DEM. It is built on a recently proposed vectorial BNPE method for estimating spatially correlated noise using noise informative areas and fractal Brownian motion. The new multivariate method is derived to estimate the effect of the stacking procedure and that of the epipolar line error on local (fine-scale) standard deviation and autocorrelation function width of photogrammetric DEM measurement error. Applying the new estimator to Advanced Spaceborne Thermal Emission and Reflection Radiometer (ASTER) GDEM2 and Advanced Land Observing Satellite (ALOS) World 3D DEMs, good agreement of derived estimates with results available in the literature is evidenced. Adopted for TanDEM-X-DEM, estimates obtained agree well with the values provided in the height error map. In future works, the proposed no-reference method for analyzing DEM error can be extended to a larger number of predictors for accounting for other factors influencing remote sensing (RS) DEM accuracy.**

***Index Terms*— Advanced Land Observing Satellite (ALOS) World 3D (AW3D), Advanced Spaceborne Thermal Emission and Reflection Radiometer (ASTER) GDEM2, blind noise parameter estimation (BNPE), digital elevation model (DEM), DEM accuracy, elevation measurement error, multivariate noise context-dependence, TanDEM-X-DEM.**

I. Introduction

GRIDDED digital elevation models (DEMs) have found applications for disaster and crisis-management support [1], urban growth monitoring and planning [2], and remote sensing (RS) image processing [3]. A DEM is subject to error that may impair its quality. This error originates from various sources, including elevation measurement method (traditional optical stereo matching, radar interferometry (IfSAR), or light detection and ranging (LiDAR) [4]), instrument, terrain structure, vegetation cover, and DEM interpolation [5], making both theoretical and experimental analyses of its properties a complicated task [6]. Only vertical DEM error is of interest in this article. In what follows, the multifactor nature of DEM error is referred as multivariate context-dependence.

DEM error leads to uncertainty in the calculation of terrain attributes such as terrain slope, aspect, or roughness. Even partial knowledge of DEM error properties and its spatial pattern is valuable [6]–[8] in such areas as DEM fusion [9], [10], filling voids [11], DEM filtering [8], [12]–[14], DEM interpolation [15], modeling of DEM error propagation [16] in hillslope erosion/failure analysis, land slide risk estimation, and hydrological modeling. Improving knowledge of DEM error was identified as a major research direction in digital terrain modeling domain [17].

The basic DEM error characteristic [8] is its RMSE $= ((1/n)\sum_{i=1}^{n}(z_{\mathrm{DEM}.i} - z_{\mathrm{Ref}.i})^2)^{1/2}$, where $z_{\mathrm{DEM}.i}$ is an elevation measurement from the DEM, $z_{\mathrm{Ref}.i}$ is the reference elevation measurement of significantly higher accuracy, and n is the number of available measurements. RMSE can be decomposed as $RMSE = (\sigma_{\mathrm{e}}^2 + M_{\mathrm{e}}^2)^{1/2}$, where mean error or bias $M_{\mathrm{e}} = (1/n)\sum_{i=1}^{n}(z_{\mathrm{DEM}.i} - z_{\mathrm{Ref}.i})$ and standard deviation (SD) $\sigma_{\mathrm{e}} = ((1/n)\sum_{i=1}^{n}(z_{\mathrm{DEM}.i} - z_{\mathrm{Ref}.i} - M_{\mathrm{e}})^2)^{1/2}$ [6]. The σ_{e} and M_{e} terms characterize the random and systematic error components, respectively. Spatial properties of DEM error are characterized by its spatial correlation function [16].

To measure DEM error characteristics, a high-quality reference DEM (e.g., created using LiDAR) or point elevation measurements (obtained by geodetic surveys) are typically utilized [7], [18], [19]. Comparison between DEMs is a complicated task. Both analyzed and reference DEMs should have the same spatial resolution, cover the same area, and share approximately the same acquisition date. The reference DEM should have significantly better accuracy than the analyzed DEM. Acquisition of such data can be expensive and is not always possible. Direct DEM comparison is further complicated for vegetation cover that can yield different elevation measurements for different instruments (optical, IfSAR, and LiDAR) [20]–[22].

Manuscript received January 14, 2018; revised February 7, 2019 and August 1, 2019; accepted October 14, 2019. *(Corresponding author: Benoit Vozel.)*

M. L. Uss and V. V. Lukin are with the Department of Information-Communication Technologies, National Aerospace University, 61070 Kharkiv, Ukraine (e-mail: uss@xai.edu.ua; lukin@ai.kharkov.com).

B. Vozel and K. Chehdi are with IETR UMR CNRS 6164, University of Rennes 1, Enssat, 22305 Lannion, France (e-mail: benoit.vozel@univ-rennes1.fr; kacem.chehdi@univ-rennes1.fr).

Color versions of one or more of the figures in this article are available online at http://ieeexplore.ieee.org.

Digital Object Identifier 10.1109/TGRS.2019.2951178

Abovementioned tight requirements on the reference DEM can be relaxed for featureless flat terrain. For a local DEM patch representing a flat terrain, $z_{\text{Ref}} = \text{const}$ and DEM SD can be directly accessed as $\sigma_{\text{e}} = ((1/n)\sum_{i=1}^{n}(z_{\text{DEM}.i} - (1/n)\sum_{i=1}^{n} z_{\text{DEM}.i})^2)^{1/2}$. In this case, reference DEM is not needed to estimate σ_{e} (however, it is still needed to estimate the DEM bias). Having enough flat patches allows collecting many local σ_{e} estimates for DEM accuracy characterization. Importantly, using flat DEM patches, SD of DEM error can be estimated in the no-reference fashion. This approach was leveraged by Becek [22]. He proposed to use runways as flat patches and estimated the bias and SD of the Advanced Spaceborne Thermal Emission and Reflection Radiometer (ASTER) global DEM2 [23], [24] (later referred to as GDEM2) and Shuttle Radar Topography Mission (SRTM) DEM [25] error.

Usage of flat terrain encounters several problems. First, flat areas are unknown beforehand (with narrow exception exploited by Becek [22]). Second, absolutely flat areas are hard to find. Let us consider the estimation of σ_{e} value locally from a DEM patch of 15×15 pixels. For GDEM2, one pixel corresponds to 30 m on the ground; the patch is, thus, 450×450 m^2. The mean σ_{e} value for GDEM2 has been shown in [22] to vary from 2 to 6 m as mean stacking number reduces from 25 to about 5. SD of a DEM patch representing a mixture of terrain elevation with SD σ_{tr} and random noise with SD σ_{e} is $\sigma_{\text{noisy.terrain}} = (\sigma_{\text{e}}^2 + \sigma_{\text{tr}}^2)^{1/2}$. To use $\sigma_{\text{noisy.terrain}}$ as an unbiased estimate of σ_{e}, the value of σ_{tr} should be a magnitude smaller than σ_{e}. For example, for $\sigma_{\text{tr}} < 0.2\sigma_{\text{e}}$, the value of $\sigma_{\text{noisy.terrain}} < 1.02\sigma_{\text{e}}$. For a low value of σ_{e}, such as $\sigma_{\text{e}} = 2$ m for GDEM2, σ_{tr} should be of the order of $0.2 \cdot 2$ m $= 0.4$ m. This implies maximum elevation variation ± 1.2 m (± 3sigma) within the patch. This restriction severely reduces the number of flat patches available for no-reference DEM error characterization, as well as their variability.

The process of estimation of DEM error SD from featureless flat terrain has a direct counterpart in image processing domain, namely, blind noise parameter estimation (BNPE) approach [26], where the goal is to estimate image sensor noise characteristics (variance or autocorrelation function) from a mixture of true signal and noise. The common solution is to find and use image homogeneous areas (HAs), where true signal is negligible as compared to sensor noise [27]. The link between no-reference DEM error characterization and BNPE problem is that flat terrain for DEM corresponds to HA for images, DEM error to sensor noise, and true signal to error-free DEM. The problem of automatic HA search is the core of BNPE approach, and many efficient solutions have been proposed. Furthermore, BNPE methodology moved beyond searching HA areas only: moderately heterogeneous areas could be used for noise parameters estimation by assuming spectral differences between noise and the true signal [26]. Therefore, BNPE methodology provides suitable approaches to two main barriers to no-reference DEM error characterization discussed above: automatic search of HA (flat DEM patches) and usage of moderately heterogeneous patches (DEM patches corresponding to moderately undulating terrain).

Going through obvious similarities underlined above, adapting key ideas from the BNPE methodology so as to make them fit the issues and problems to solve for gridded DEM is the main contribution of this article. The main difficulty lies in multivariate context-dependence of DEM error compared to the univariate dependence of sensor noise on image intensity widely considered in the BNPE domain. (This issue is discussed more in detail in Section II). To the best of authors' knowledge, the only blind noise parameter estimator designed to deal with the multivariate context-dependent error was proposed by Uss *et al.* [28] and called multivariate, vector estimator of spatially correlated noise using noise informative (NI) areas and fractal Brownian motion (mvcNI+fBm). Therefore, in this article, we modify and evolve mvcNI+fBm estimator to make it adjusted to DEM data and apply it to two global photogrammetric gridded DEMs: GDEM2 and Advanced Land Observing Satellite (ALOS) Global Digital Surface Model "ALOS World 3D" (AW3D) with a 5-m spacing [29] and 30-m spacing (AW3D30) [30], and IfSAR DEM TanDEM-X-DEM [31]. In regard to the complexity of DEM error as compared to pure sensor noise, we devote significant efforts to explain and interpret the meaning of estimates obtained with the proposed approach.

The remainder of this article is structured as follows. In Section II, we start by discussing possible sources of error in DEM. Then, we establish that sensitivity to fine-scale error offered by BNPE methodology is fully beneficial to fine-scale elevation measurement error. Section III introduces the mathematical model of the DEM measurement error and several bivariate regression models for the measurement error variance and spatial correlation width. Section IV details the necessary information on the mvcNI+fBm estimator. In Section V, the experimental section, the mvcNI+fBm is used to select the most relevant DEM measurement error model and estimate its coefficients using GDEM2, AW3D30, AW3D, and TanDEM-X-DEM data. It is demonstrated that obtained DEM error models are physically adequate and in good agreement with the respective DEM accuracy analysis published in the literature. On the basis of these promising results, concluding remarks and future work are given.

II. DEM Error Model

An instrument (sensor) measures elevation at discrete, possibly irregular spaced points on the earth surface. To form a gridded DEM, discrete measurements are interpolated at nodes on a regular grid: $\hat{Z}_{\text{grid}}(x_t, y_s) = \hat{Z}_{\text{grid}}(t, s)$, where $x_t = x_0 + t \cdot r_{\text{DEM}}$, $y_s = y_0 + s \cdot r_{\text{DEM}}$, r_{DEM} is the grid step or DEM spatial resolution, and (x_0, y_0) is the grid origin.

The measured elevation is a coarsened representation of the actual terrain because of the finite instrument spatial resolution (correlation window support in photogrammetric DEM and sounding beam footprint in IfSAR and LiDAR). Elevation measurement process is subject to measurement errors (Fig. 1). For bare soil, the instrument introduces error related to its positioning/orientation accuracy, disparity estimation errors, higher or lower correlation between stereo images, stacking number, epipolar line error in photogrammetric DEM, phase unwrapping errors in IfSAR, and the time-of-delay

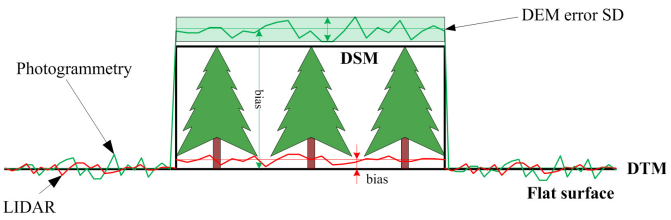

Fig. 1. Illustration of the DEM error structure.

measurement accuracy in LiDAR [6], [7], [22], [32], [33]. This error source was called instrument-induced in [22]. The bias and SD of this error could depend on terrain morphological attributes such as slope, aspect, and roughness [8]. Vegetation canopy is additional source of DEM error [32]. For example, optical sensors measure elevation at the canopy top, LiDAR could measure both the vegetation canopy top (the first return) and ground surface (the last return), and IfSAR measures intermediate elevation between the vegetation canopy top and the ground surface [8], [19]. In [4], it was demonstrated that both bias and SD of SRTM DEM error significantly increase in areas covered by natural forests as compared to grassland pastures and agricultural areas. The error related to terrain surface properties was called environment-induced in [22]. Finally, interpolation and quantization errors are added. Gridded DEM error may exhibit spatial correlation that should be taken into account as well [6], [7], [33]. In what follows, we refer to factors/attributes influencing DEM error as error predictors and denote them by $p_1, p_2, \ldots, p_{N_p}$, where N_p is number of predictors. In the vector form, predictor vector is defined as $\mathbf{p} = (p_1, p_2, \ldots, p_{N_p})$. Dependence of DEM error parameters (SD in particular) on multiple predictors is the essence of multivariate context-dependence.

Therefore, the values of gridded DEM can be represented as $\hat{Z}_{\text{grid}}(t,s) = Z_{\text{grid}}(t,s) + e_{\text{grid.mes}}(t,s,\mathbf{p}(t,s))$, where $Z_{\text{grid}}(t,s)$ is the error-free DEM and $e_{\text{grid.mes}}(t,s,\mathbf{p}(t,s))$ is the DEM measurement error. In this article, we treat the difference $Z_{\text{true}}(t,s) - Z_{\text{grid}}(t,s)$ between the actual elevation $Z_{\text{true}}(t,s)$ and error-free DEM not as error, but as uncertainty [6] that depends on the relation between DEM spatial resolution and terrain characteristic size and DEM interpolation method. By DEM error analysis, we understand the study of $e_{\text{grid.mes}}(t,s,\mathbf{p}(t,s))$ measurement error term.

To evaluate the DEM error, many researchers have used residuals $r(t,s) = \hat{Z}_{\text{grid}}(t,s) - \hat{Z}_{\text{grid.ref}}(t,s)$ between the analyzed DEM and a more accurate reference DEM. The drawback of this approach is that the reference DEM has its own errors that not always could be neglected [34]. The residual $r(t,s) = [Z_{\text{grid}}(t,s) - Z_{\text{grid.ref}}(t,s)] + [e_{\text{grid.mes}}(t,s,\mathbf{p}(t,s)) - e_{\text{grid.ref.mes}}(t,s,\mathbf{p}_{\text{ref}}(t,s))]$ comprises two error terms. For the first term—difference between error-free DEMs—to be negligible, both DEMs should have the same spatial resolution and perfect spatial alignment (the absence of planimetric errors) [35]. The second term includes errors of both analyzed and reference DEMs. To minimize the influence of the reference DEM error, this DEM should be obtained with an order of magnitude accurate instrument free from vegetation canopy and terrain surface parameters influence. Analysis of residuals complicates further if analyzed and reference DEMs were collected with a time lag because of terrain dynamics, vegetation change (leaf-on, leaf-off conditions [34]), among other factors. The problem remains how to characterize error of an accurate DEM when finding a sufficiently accurate reference DEM is impossible.

In this article, we investigate the possibility of characterizing DEM error without the use of any reference DEM, but relying on noisy measurements $\hat{Z}_{\text{grid}}$ themselves. This problem is known in image processing domain as BNPE problem, and it basically aims at estimating random noise characteristics (variance and autocorrelation function parameters) from a mixture of noise-free image and noise, i.e., noisy image [26]. From image processing point of view, the DEM $\hat{Z}_{\text{grid}}$ is a noisy single-component image, Z_{grid} is the noise-free image, and $e_{\text{grid.mes}}$ is the noise term. In what follows, we analyze what terms of DEM error are accessible by BNPE. Such a preliminary analysis is essential to correctly interpret the results obtained by the mvcNI+fBm estimator derived for real DEMs.

To illustrate better the connection between DEM error characterization and BNPE problems, let us discuss more in detail the "runway" method proposed by Becek [22], [36]. According to it, if we assume that for a particular DEM patch, the reference DEM is flat, the variance of residual between analyzed and reference DEMs is composed of instrumental (σ_I^2) and environmental (σ_e^2) components and undesirable target-induced component σ_T^2 that is caused by the unaccounted terrain roughness: $\sigma_Z^2 = \sigma_I^2 + \sigma_e^2 + \sigma_T^2$. The value σ_T^2 can be approximated as $\sigma_T^2 = (1/12) r_{\text{DEM}}^2 \tan^2(\alpha) + (1/12) q^2$, where α is the terrain root mean square slope and q is the quantization step [22]. For a flat terrain (e.g., runway), $\alpha \approx 0$ and target-induced term becomes negligible. In the above introduced terms, for flat terrain, $Z_{\text{grid}}(t,s) = Z_{\text{grid}} = \text{const}$, $\hat{Z}_{\text{grid.ref}}(t,s) == Z_{\text{grid.ref}}(t,s) = Z_{\text{grid.ref}} = \text{const}$, $e_{\text{grid.ref.mes}}(t,s,\mathbf{p}_{\text{ref}}(t,s)) = 0$, and $r(t,s)$ simplifies to $[Z_{\text{grid}} - Z_{\text{grid.ref}}] + e_{\text{grid.mes}}(t,s,\mathbf{p}(t,s))$. Even not knowing the actual evaluation $Z_{\text{grid.ref}}$, variance of DEM error can be directly estimated as follows:

$$\begin{aligned}&\text{Var}(e_{\text{grid.mes}}(t,s,\mathbf{p}(t,s)))\\ &\quad = \text{Var}(\hat{Z}_{\text{grid}}(t,s) - Z_{\text{grid.ref}}) = \text{Var}(\hat{Z}_{\text{grid}}(t,s)).\end{aligned} \quad (1)$$

This idea directly corresponds to the so-called HA approach, which is the simplest BNPE approach [27]. The limiting factors of the "runway" method is that: 1) it still relies on reference data to locate flat terrain patches; 2) number of flat patches provided by this method is limited; 3) these patches represent only one particular terrain class—concrete surfaces, and cannot, in principle, be extended to other terrain classes; and 4) (1) requires absolutely flat patches that is hard to satisfy. These limitations have been overcome in advanced BNPE methods that provide means for automatic search of HA and ability to deal with moderately heterogeneous patches. Thus, for global DEMs, BNPE could potentially rely on a larger amount of data for analyzing DEM error and cover larger variety of DEM error predictors.

BNPE has seen fast development in the last decade and now provides a mature set of methods applicable to a variety of scenarios [26]: single channel [37], multispectral (or color) [38], and hyperspectral images [39], [40]; optical [41] and radar [42] images; signal-independent (additive) [37], Poisson [43], multiplicative noise [42], or their mixture in the form of general model with signal-dependent noise variance [38], [44]–[46]; methods with ability to characterize only noise variance [37]–[45] as well as noise spatial correlation properties [46], [47]. Accuracy of these methods is high enough to consider them as an alternative to direct sensor calibration [38]–[40], [43], [45].

The BNPE problem is ill-conditioned and requires additional *a priori* information on noise and noise-free image properties to be solved reliably. Such additional information could originate from either spatial [27] or spectral [48] domains leading to two main groups of BNPE methods working in spatial or spectral domain, respectively. Spatial *a priori* information assumes that noise and noise-free image could be separated in image HA, where noise-free image level variation is negligible as compared to noise. Spectral *a priori* information assumes that noise-free image and noise difference in spectral domain could help their separation. The state-of-the-art methods typically utilize both spatial and spectral information; the mvcNI+fBm method also belongs to this group. Irrespectively from *a priori* information used, BNPE methods operate by finding image patches where noise-free image and noise can be separated in the best way and locally estimating noise variance from such patches [26].

To illustrate how moderately heterogeneous patches can be used for BNPE problem and which components of DEM error can be estimated by this approach, it is useful to represent BNPE as a high-pass filter. The value of $\mathrm{Var}(\hat{Z}_{\mathrm{grid}}(t,s)) = (1/N^2)\sum_{i,j=1}^{i,j\le N}(\hat{Z}_{\mathrm{grid}}(t,s) - (1/N^2)\sum_{i,j=1}^{i,j\le N}\hat{Z}_{\mathrm{grid}}(t,s))^2$ is the local variance of residuals $\hat{Z}_{\mathrm{grid}}(t,s) - (1/N^2)\sum_{i,j=1}^{i,j\le N}\hat{Z}_{\mathrm{grid}}(t,s)$ between DEM $\hat{Z}_{\mathrm{grid}}(t,s)$ and its low-pass filtered version $(1/N^2)\sum_{i,j=1}^{i,j\le N}\hat{Z}_{\mathrm{grid}}(t,s)$. Here, N is the linear patch size. The difference between signal and its low-pass filtered version is equivalent to a high-passed filter applied to the signal. The error-free elevation has multiscale property and possesses fine-, meso-, as well as macroscale-variations [49]. In contrast, instrument-induced error has slow-varying bias component caused by instrument calibration errors (orientation error and jitter noise) and exhibits random fluctuations at the fine scale. Environment-induced error is related to the terrain surface and could borrow at some extent its multiscale structure. High-pass filter suppresses constant term and large-scale elevation variations and keeps only fine-scale details. This procedure partly removes error-free DEM variations making some of moderately heterogeneous patches almost homogeneous and suitable for estimating DEM error through BNPE; the error-free DEM and error bias terms are also removed as well as low-frequency calibration error; large-scale environment-induced variations of DEM error (bias between bare soil DEM and terrain with vegetation cover) are likewise filtered-out. In contrast, fine-scale random variations of DEM error

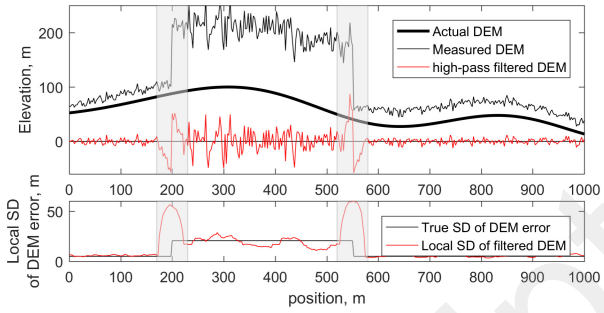

Fig. 2. Illustration of the local DEM error structure. Heterogeneous areas are marked by gray fill.

(both instrument- and environment-induced) pass through the high-pass filter. This is illustrated in Fig. 2 where a terrain surface and DEM error are simulated. After high-pass filtering, HA areas represent fine-scale component of DEM error. Heterogeneous areas (shown by gray in Fig. 2) do not represent DEM error, should be detected, and removed from further consideration. In other words, BNPE can be viewed as a filtering process that separates a DEM error from the actual DEM using difference in their autocorrelation functions.

Let us summarize BNPE properties important for understanding effect of their application to gridded DEM: 1) it does not require any reference image (DEM); 2) it characterizes image noise (DEM error) locally; 3) it employs spatial (HAs) and spectral (different autocorrelation functions of the true signal and noise) separability of true signal (error-free DEM) and noise (DEM error); 4) it performs automatic search of image patches where the true signal (error-free DEM) and noise (DEM error) are separable at an extent allowing noise (DEM error) parameters estimation; and 5) it estimates only fine-scale random noise (DEM error) component, and bias and large-scale components cannot be estimated. Therefore, BNPE methods are able to estimate local SD of fine-scale component of DEM measurement error. This error is similar to the residual error or leveled error introduced in [50] that indicates the best possible DEM error with no instrument orientation error affecting the result.

In the majority of BNPE methods, noise can be represented as the sum of two terms: a signal-independent or additive and signal-dependent one. In RS applications, the additive noise is sensor noise (e.g., thermal noise), and it does not depend on the sensed image. The signal-dependent noise is due to the physical nature of measured quantity (e.g., photon-counting or Poisson noise in optical images, and coherent speckle noise in synthetic aperture radar images), and its variance is a linear or nonlinear function of sensed image intensity [51], [52]. Therefore, this observation noise model is univariate. In contrast, DEM error depends on many predictors both instrument- and environment-related. To the best of authors' knowledge, the only BNPE method able to deal with the multivariate noise model is the recently proposed mvcNI+fBm (see Section IV for details). This property has determined our choice in favor of this estimator for characterizing the DEM error.

Including all significant predictors selected for analysis in predictor vector $\mathbf{p}$, one expects DEM error to exhibit

the same statistical properties for all patches with the same predictor vector. However, not all predictors could be observed, identified, or considered in a particular study. Therefore, predictor vector is split into observable and not-observable, latent, parts: $\mathbf{p} = (\mathbf{p}_{\text{observed}}, \mathbf{p}_{\text{latent}})$. The mvcNI+fBm is designed to estimate measurement error SD σ_{e} for patches with similar observable predictors $\mathbf{p}_{\text{observed}}$. However, latent predictors are not controlled leading to variations of the estimates SD: $\hat{\sigma}^2_{e.i} = \hat{\sigma}^2_{\text{e}}(\mathbf{p}_{\text{observed}}, \mathbf{p}_{\text{latent}.i})$, where $i = 1 \ldots N_{\text{pt}}$, N_{pt} is the number of patches. In the simplest case, final SD estimates are obtained as average over all patches: $\hat{\sigma}^2_{\text{e}} = N_{\text{pt}}^{-1} \sum_{i=1}^{N_{\text{pt}}} \hat{\sigma}^2_{e.i}(\mathbf{p}_{\text{observed}}, \mathbf{p}_{\text{latent}.i}) \approx \hat{\sigma}^2_{\text{e}}(\mathbf{p}_{\text{observed}}, \bar{\mathbf{p}}_{\text{latent}})$, where $\bar{\mathbf{p}}_{\text{latent}} = N_{\text{pt}}^{-1} \sum_{i=1}^{N_{pt}} \mathbf{p}_{\text{latent}.i}$. The mvcNI+fBm estimates error parameters for a fixed value of observable predictors and an average value of the latent ones.

Significant limitation of BNPE resides in its operation principle. As DEM error SD is estimated from homogeneous or moderately heterogeneous DEM patches representing low relief terrain, predictor vector values that correspond to high relief terrain are inaccessible. Primarily, DEM error parameters for patches with high-slope SD cannot be estimated using the no-reference approach. Homogeneity level required for reliable DEM error SD estimation is related to the DEM error SD itself: the lower the DEM error is, the more homogeneous patches are needed to access it. The DEM error component accessible by the BNPE methods can be finally formulated as fine-scale measurement error SD in low-relief areas averaged over latent, unobservable predictors. In what follows, we refer to this DEM error component simply as measurement error or even error, omitting other qualifiers.

III. Elevation Measurement Error Model

A. Mathematical Model of DEM Error

Following the discussion in Section II, for an $(2N_h + 1) \times (2N_h + 1)$ DEM patch, we assume the following model:

$$\hat{Z}_{\text{grid}}(t, s) = Z_{\text{grid}}(t, s) + e_{\text{grid.mes}}(t, s, \mathbf{p}) \tag{2}$$

where $t, s = -N_h, \ldots, N_h$ denote pixel coordinates within the patch, N_h is the patch half size, $N = 2N_h + 1$ is the patch linear size, $\hat{Z}_{\text{grid}}(t, s)$ and $Z_{\text{grid}}(t, s)$ are affected by errors and error-free DEMs, and $e_{\text{grid.mes}}(t, s, \mathbf{p})$ is a zero-mean spatially correlated random error that models the fine-scale measurement error. For a particular patch, the predictor vector $\mathbf{p}$ is assumed constant but changing its value from patch to patch. Model (2) resembles DEM modeling in geostatistics when a DEM patch is split into zero-mean error term and spatially autocorrelated random field modeling error-free DEM [8].

It is assumed that error is uncorrelated with the error-free DEM. By this, we mean that only error parameters are dependent on DEM structure and not error realization itself, i.e., error and error-free elevation values in the same pixel have no linear relationship with each other. The Gaussian distribution is the most natural assumption for DEM error, which is generated by a complex mixture of many factors. The validity of this distribution has been reported in many sources [4], [6], [7], [10], [33].

In addition, the semivariogram analysis of DEM error indicates the presence of spatial autocorrelation [7], [33]. At the lag distances considered in this article (below 100–200 m), isotropy of DEM errors is also typically assumed. (Anisotropy of DEM errors was reported in [33] for lag distances exceeding 500 m.) With this, no strong evidence supporting a particular spatial autocorrelation function shape is present in the available literature. We performed experiments with two widely used correlation function shapes: exponential $R_{\text{e}}(t_1, s_1, t_2, s_2) = \sigma^2_{\text{e}}(\mathbf{p}) \exp(-(|d|/\sigma_{\text{Corr}}(\mathbf{p})))$ [16] and Gaussian $R_{\text{e}}(t_1, s_1, t_2, s_2) = \sigma^2_{\text{e}}(\mathbf{p}) \exp(-(d^2/2\sigma^2_{\text{Corr}}(\mathbf{p})))$, where $d = ((t_2 - s_1)^2 + (t_2 - s_1)^2)^{1/2}$, $\sigma^2_{\text{e}}(\mathbf{p})$ is the noise variance, and $\sigma^2_{\text{Corr}}(\mathbf{p})$ is the parameter that characterizes unknown error spatial correlation width (σ_{Corr} is the distance in pixels where error correlation drops to a certain value, 0.6 for Gaussian shape, and 0.37 for exponential shape). It was found that the Gaussian shape is more adequate than exponential one (in terms of regression quality measured by R-square, see Section V) for GDEM2 and AW3D30 global DEMs, but exponential model is more suitable for TanDEM-X-DEM.

The DEM error properties accepted in the mvcNI+fBm can be summarized as follows: normal distribution, stationary fine-scale error with Gaussian isotropic spatial correlation function, and uncorrelated with the error-free DEM. The goal of the mvcNI+fBm estimator is to evaluate types and coefficients of regression functions $\sigma^2_{\text{e}}(\mathbf{p})$ and $\sigma^2_{\text{Corr}}(\mathbf{p})$ using the large number of $\hat{Z}_{\text{grid}}$ patches.

The error-free DEM is modeled as a fractal surface, namely, nonstationary 2-D fBm [53]. The fBm model is suitable for describing the earth surface that was shown to fulfill the multiscale, fractal properties [49], [54], [55]. According to the fBm model, the error-free DEM increments $\Delta Z(t, s) = Z(t, s) - Z(0, 0)$ with respect to the patch central pixel $Z(0, 0)$ represent a nonstationary random Gaussian process with covariation matrix

$$\begin{aligned} R_Z(t_1, s_1, t_2, s_2) &= \langle \Delta Z(t_1, s_1) \cdot \Delta Z(t_2, s_2) \rangle \\ &= 0.5\sigma_x^2 \big(\big(t_1^2 + s_1^2\big)^{H_q} + \big(t_2^2 + s_2^2\big)^{H_q} \\ &\quad - ((t_1 - t_2)^2 + (s_1 - s_2)^2)^{H_q} \big). \end{aligned}$$

where $H_q \in (0,1)$ is the Hurst exponent describing fBm-field roughness ($H_q \to 0$ relates to a rougher terrain, $H_q \to 1$ to a smoother one), and σ_x describes the fBm amplitude as SD of elevation increments on unit distance. The covariation matrix of measured increments $\Delta\hat{Z}(t, s) = \hat{Z}(t, s) - \hat{Z}(0, 0)$ can be shown to have the following form:

$$\begin{aligned} R_{\hat{Z}}(t_1, s_1, t_2, s_2) &= \langle \Delta\hat{Z}(t_1, s_1) \cdot \Delta\hat{Z}(t_2, s_2) \rangle \\ &= R_Z(t_1, s_1, t_2, s_2) + R_{\text{e}}(t_1 - t_2, s_1 - s_2) \\ &\quad + R_{\text{e}}(0, 0) - R_{\text{e}}(t_1, s_1) - R_{\text{e}}(t_2, s_2). \end{aligned} \tag{3}$$

B. Bivariate Model of Measurement Error Variance and Correlation

Among the multitude of factors influencing the DEM error, in this article, we have considered only two instrument-induced factors valid for photogrammetric DEMs: the stacking number and epipolar line error.

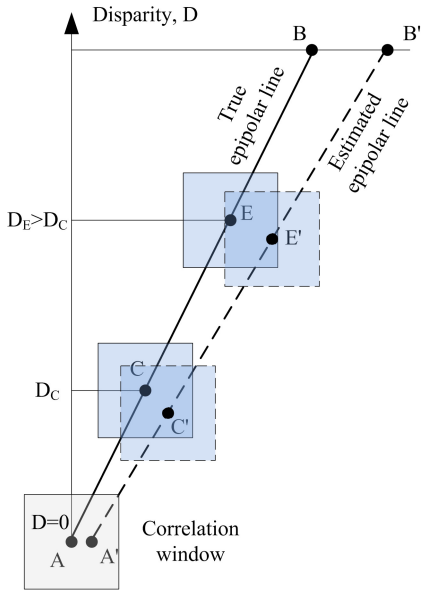

Fig. 3. Illustration of epipolar line error.

Stacking is aggregation of data obtained from multiple passes of the instrument. Stacking number, N_{stk}, is the number of image stereo pairs used to estimate elevation. It is selected here as the first predictor of DEM error: $p_1 = N_{\text{stk}}$. Conceptually, measurement error variance should decrease as N_{stk}^{-1} due to averaging over stack of DEM images. According to this model, σ_{e}^2 should converge to zero with N_{stk} approaching infinity, which is not realistic due to finite correlation kernel (window) size [56]. Therefore, we consider more adequate model $\sigma_{\text{e}}^2 = 1 + N_{\text{stk}}^{-1}$ (in what follows, we represent regression models in simplified form by setting model coefficients to unity).

In stereovision and photogrammetry, finding elevation of a terrain object consists in 1-D search of the object image on the left(right) image along the corresponding epipolar line at the right(left) image. The epipolar line on one stereo pair image is formed by projecting all 3-D points having the same projection in the other stereo pair image [57]. The object displacement (with respect to a reference elevation, typically $Z = 0$) along the epipolar line is called disparity D, which is related to elevation as $Z = D(r/B)$, where B denotes the base-to-height ratio and r is an instrument spatial resolution [58]. In Fig. 3, elevation $Z = 0$ corresponds to point A and line A–B is the corresponding epipolar line. Object E has higher elevation (and disparity) than object C and is placed farer from point A along the epipolar line. Position of the reference point A and orientation of the epipolar line are determined from the instrument calibration data and are subject to errors. The deviation of the estimated epipolar line from the true one is called epipolar line error [58]. It has been shown that camera errors propagate to epipolar line error in a way dependent on disparity [59]. As a result, SD of distance between points on the true and estimated epipolar lines is increasing with disparity: in average $\|A - A'\| < \|C - C'\| < \|D - D'\| < \|B - B'\|$. The object disparity is found by maximizing correlation between left and right stereo images within the search window moving along the epipolar line. As estimated epipolar line deviates from its true position, the value of correlation drops, correlation profile maximum smears, and disparity estimation accuracy decreases. In this manner, σ_{e}^2 becomes dependent on D and consequently on elevation Z. We, therefore, select elevation Z as the second predictor of DEM error: $p_2 = Z$.

Obviously, the influence of epipolar line error depends on the accuracy of an instrument onboard calibration data. In Section V, we show that ASTER GDEM2 with calibration data of relatively low accuracy [58] demonstrates the strong influence of elevation on DEM error. On the contrary, for AW3D and AW3D30 DEMs with calibration data of relatively high accuracy [60], this dependence is not observed.

In the absence of exact model of epipolar line error influence on σ_{e}^2, we propose to model it in the form $1 + Z^m$, where m takes values 1 or 2 in this study (formalizing linear and quadratic dependence hypotheses of measurement error parameters on elevation).

Combining the two univariate terms $1 + N_{\text{stk}}^{-1}$ and $1 + Z^m$, we get for σ_{e}^2 a bivariate model in the form $(1 + Z^m) + (1 + Z^m)N_{\text{stk}}^{-1} = 1 + N_{\text{stk}}^{-1} + Z^m + Z^m N_{\text{stk}}^{-1}$, leading to the following expression:

$$\sigma_{\text{e}}^2(\mathbf{p}, \boldsymbol{\theta}_{\text{e}}) = \sigma_{\text{Var01}}^2 + \sigma_{\text{Var02}}^2 N_{\text{stk}}^{-1} + c_{\text{VarZ1}} Z^m + c_{\text{VarZ2}} Z^m N_{\text{stk}}^{-1} \tag{4}$$

where $\mathbf{p} = (N_{\text{stk}}, Z)$, $N_{\text{p}} = 2$ is a 2-D predictor vector, and $\boldsymbol{\theta}_{\text{e}} = (\sigma_{\text{Var01}}^2, \sigma_{\text{Var02}}^2, c_{\text{VarZ1}}, c_{\text{VarZ2}})$ is the DEM error variance parameter vector.

In (4), $\sigma_{\text{Var01}}^2 + c_{\text{VarZ1}} Z^m$ component is shared by all DEM realizations in the stack and related to the underlying surface properties. This error component can be viewed as measurement error of DEM obtained from noise-free stereo images. The term $\sigma_{\text{Var02}}^2 + c_{\text{VarZ2}} Z^m$ is the variance of component that is uncorrelated between DEM realizations in the stack (due to different sensor noise realizations in each stereo pair and different viewing geometries).

For photogrammetric DEM, measurement error spatial correlation width is related to the correlation peak sharpness and should not exceed correlation window size. The value of σ_{Corr}^2 is supposed not to change from one stereo pair to another one. The averaging over stereo pairs does not affect σ_{Corr}^2 of random components and could slightly increase it as a result of spatial smoothing due to horizontal registration error of stereo pairs. Therefore, σ_{Corr}^2 could slightly increase with N_{stk}. As epipolar line error smears correlation peak, σ_{Corr}^2 is expected to increase with elevation.

We propose to use the same model for σ_{Corr}^2 as for σ_{e}^2

$$\sigma_{\text{Corr}}^2(\mathbf{p}, \boldsymbol{\theta}_{\text{Corr}}) = \sigma_{\text{Corr01}}^2 + \sigma_{\text{Corr02}}^2 N_{\text{stk}}^{-1} + c_{\text{CorrZ1}} Z^m + c_{\text{CorrZ2}} Z^m N_{\text{stk}}^{-1}. \tag{5}$$

where $\boldsymbol{\theta}_{\text{Corr}} = (\sigma_{\text{Corr01}}^2, \sigma_{\text{Corr02}}^2, c_{\text{CorrZ1}}, c_{\text{CorrZ2}})$ is the DEM error correlation width parameter vector.

In addition to full models (4) and (5), we have also considered two simpler submodels for both σ_{e}^2 and σ_{Corr}^2. The first submodel uses only predictor N_{stk}, and the second one employs only Z. Taking into account two possible values for m (1 or 2), we obtain a set of six alternative models to test for

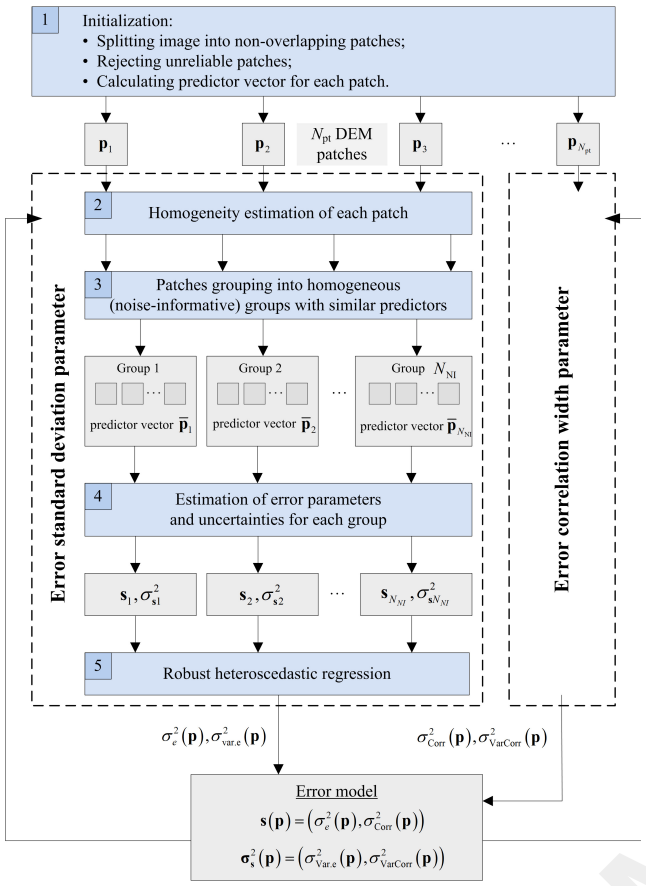

Fig. 4. Processing pipeline of the mvcNI+fBm method.

the DEM measurement error parameters: 1, $1 + N^{-1}_{\text{stk}}$, $1 + Z$, $1 + Z^2$, $1 + N^{-1}_{\text{stk}} + Z + ZN^{-1}_{\text{stk}}$, and $1 + N^{-1}_{\text{stk}} + Z^2 + Z^2N^{-1}_{\text{stk}}$. In what follows, we use the mvcNI+fBm both to select the most relevant model for each considered DEM and estimate the corresponding model coefficients.

IV. No-Reference Estimation of Measurement Error Parameters: the mvcNI+fBm Estimator

A. Generalized Description of the Adapted mvcNI+fBm Estimator of DEM Error Parameters

The main processing stages of the mvcNI+fBm method include: 1) initialization; 2) patches homogeneity estimation; 3) grouping of image patches; 4) processing of the formed groups; and 5) multivariate estimation of context-dependent error parameters (see Fig. 4) [28]. In the mvcNI+fBm method, homogeneity estimation stage depends on DEM error parameters; therefore, iterative repeating of stages (2)–(5) is required. Originally, the mvcNI+fBm was proposed for vector RS images. In this article, it is adapted to the case of gridded DEM images that represents single-channel data. Let us consider each stage of the mvcNI+fBm in more detail.

To estimate each error parameter, one specific call of sequence of stages (2)–(5) is performed. During each call, one parameter is fixed while the other ones are estimated, and vice-versa. For the purpose of clarity, we describe below the proposed estimation procedure for an arbitrary error parameter s, meaning either noise SD, $s = \sigma_{\text{e}}$, or spatial correlation width, $s = \sigma_{\text{Corr}}$.

At the initialization stage, the image to process is split into nonoverlapping patches. Each patch represents a group of adjacent pixels of size $N \times N$ pixels. The patches with known unreliable data are removed from further consideration. This stage is application-specific and is described in Section V. Overall number of retained patches is referred to as N_{pt}.

In the mvcNI+fBm, homogeneity index is measured as a ratio between lower bound on parameter s estimation SD (Cramér–Rao lower bound, CRLB), σ_s, and parameter value: $r_{\text{HA}} = \sigma_s/s$. For homogeneous patches, it takes low values. For example, for SD parameter, very homogeneous patches represent pure DEM error, $\sigma_{\sigma^2_{\text{e}}}$ approaches to SD of sample variance: $\sigma_{\sigma^2_{\text{e}}} \approx \sigma_{\text{e}}(2/(N^2 - 1))^{1/2}$, and $r_{\text{HA}} \approx (2/(N^2 - 1))^{1/2}$. For $N = 11$ used in Section V, $(2/(N^2 - 1))^{1/2} = 0.129$. For heterogeneous patches, where actual DEM and DEM errors cannot be separated, both σ_s and r_{HA} ratio increase. In extreme cases, for very rough patches $r_{\text{HA}} \to \infty$. The value of r_{HA} indicates how much information about error parameter s can be extracted from a given patch with patch homogeneity increasing as r_{HA} decreasing. Correspondingly, in the mvcNI+fBm, HAs with low r_{HA} index were called NI. Homogeneity estimation stage involves the estimation of error-free DEM parameters, value of σ_s, and, finally, the value of r_{HA} for each patch (see Section IV-B for details). Notice that a specific value of r_{HA} is defined for each considered error parameter. Therefore, homogeneity estimation stage (and subsequent stages of mvcNI+fBm) is repeated for each error model parameter.

Let us consider two patches with the same error parameter s and CRLBs σ_{s1} and σ_{s2}. The two patches considered together provide more information on s than each of them considered individually. By joint processing of two patches, CRLB value could be potentially reduced to $\sigma_s = \sigma_{s1}\sigma_{s2}/(\sigma_{s1} + \sigma_{s2}) < \min(\sigma_{s2}, \sigma_{s1})$. Therefore, for two patches, $r_{\text{HA}} < \min(r_{\text{HA1}}, r_{\text{HA2}})$. From this point of view, several patches considered together are "more homogeneous" and more "NI" than each of them. For a group of N_{group} patches with similar DEM properties, homogeneity index decreases approximately as $1/(N_{\text{group}})^{1/2}$. The mvcNI+fBm utilizes this property by grouping homogeneous and moderately heterogeneous patches with similar predictor values into even more homogeneous groups. Each group is further processed as a whole. In this manner, even moderately heterogeneous patches could form a homogeneous group, thus relaxing requirement to actual DEM variability and increasing number of individual error parameter estimates.

The grouping stage splits all available patches into cells with similar predictor values (implying similar error properties). Similarity of predictors is measured as $d(\mathbf{p}_1, \mathbf{p}_2) = (\sum_{j=1}^{N_{\text{p}}} w_j^2 \cdot (\mathbf{p}_1(j) - \mathbf{p}_2(j))^2)^{1/2}$, where w_j is the associated weight. Weights w_j, $j = 1, \ldots, N_{\text{p}}$, serve two interdependent goals: the first one is to limit the error parameter variation within the group and the second one is to assure the desired resolution with respect to predictors. To provide resolution

Δp_j with respect to jth predictor, the weight should be set as $w_j = \Delta p_j^{-1}$ (the used weight values for the DEM error parameter estimation are specified in Section V). In each cell, patches are sorted in the ascending order of r_{HA} value (from the most homogeneous to the most heterogeneous ones). Patches are sequentially assigned to groups. The groups are considered homogeneous when r_{HA} drops below the threshold value of 0.15 and $N_{\mathrm{group}} < 15$. (A larger size of a homogeneous group means that the set of patches in the group is more heterogeneous and consequently extracting error parameters from such a group may become less reliable; in the tests carried out later in Section V, we found 15 to be a reasonable group size.) We define by N_{NI} the number of the found NI groups. For the ith group, mean value of predictor vector $\bar{\mathbf{p}}_i$ is calculated.

At the next stage (4) of processing the formed groups, for an ith group, a single error parameter s_i ($\sigma^2_{\mathrm{e},i}$ or $\sigma^2_{\mathrm{Corr},i}$) is estimated using all patches in this group. Thus, each group provides one observation $\hat{s}_i$ of the error parameter s_i for a given value of predictor vector $\bar{\mathbf{p}}_i$. Note that the lower bound on $\hat{s}_i$ estimation error, denoted by $\sigma^2_{s_i}$, is derived as an additional output of the estimation procedure (see Section III-B).

The final stage (5) of estimation of multivariate context-dependent error parameter s mathematically corresponds to the associated robust, multivariate, heteroscedastic regression problem so as to estimate s as a function of its predictors [28]. Multivariate linear regression (nonlinear regression can be applied in a similar way) is, thus, used in the mvcNI+fBm rather than simple univariate linear regression typically considered in the past for signal-dependent noise parameter estimation. Robustness is needed to cope with gross DEM errors (outliers and blunders) [6].

B. Mathematical Details of the mvcNI+fBm Estimator

Let us formally introduce the mvcNI+fBm estimator. Using the definitions of Section III-A, the log-likelihood function of image intensities within a single patch is given by

$$\ln L(\Delta\hat{\mathbf{Z}};\theta) = -\frac{1}{2}\left[\Delta\hat{\mathbf{Z}}^T\mathbf{R}^{-1}_{\Delta\hat{\mathbf{Z}}}\Delta\hat{\mathbf{Z}} + \ln|\mathbf{R}_{\Delta\hat{\mathbf{Z}}}|\right] \tag{6}$$

where $\Delta\hat{\mathbf{Z}}$ is an $N^2 \times 1$ sample composed of all $\Delta\hat{Z}(t,s)$ within the patch, kth $\Delta\hat{\mathbf{Z}}$ element and patch pixel with coordinates (t_k, s_k) are related to each other by $k = t_k + Ns_k + N_h(N+1) + 1$, and $\boldsymbol{\theta} = (\sigma_x^2, H_q, \sigma_{\mathrm{e}}^2, \sigma^2_{\mathrm{Corr}})$ denotes the full parameter vector characterizing both error-free DEM and DEM error.

The information contained in the sample $\Delta\hat{\mathbf{Z}}$ is characterized by the Fisher information matrix (FIM) $\mathbf{I}_{\boldsymbol{\theta}}$ with elements $I_{\theta_i\theta_j} = (1/2)\mathrm{tr}(\mathbf{R}^{-1}_{\Delta\hat{\mathbf{Z}}}(\partial\mathbf{R}_{\Delta\hat{\mathbf{Z}}}/\partial\theta_i)\mathbf{R}^{-1}_{\Delta\hat{\mathbf{Z}}}(\partial\mathbf{R}_{\Delta\hat{\mathbf{Z}}}/\partial\theta_j))$, $i, j = 1, \ldots, 4$ [61].

Before estimating error parameters, we first need to determine error-free DEM parameters, σ_x^2 and H_q, using the following estimator:

$$\left[\hat{\sigma}_x^2, \hat{H}_q\right] = \underset{\sigma_x^2\geq 0, 0<H_q<1, \sigma_{\mathrm{e}}^2=\hat{\sigma}_{\mathrm{e}}^2, \sigma^2_{\mathrm{Corr}}=\hat{\sigma}^2_{\mathrm{Corr}}}{\arg\min} [\ln L(\Delta\hat{\mathbf{Z}};\boldsymbol{\theta})]. \tag{7}$$

In (7), we specify that error parameters are fixed at this stage at their current estimated values $\hat{\sigma}_{\mathrm{e}}^2$ and $\hat{\sigma}^2_{\mathrm{Corr}}$. Error-free DEM parameter estimates are only reliable for patches with ratio $\sigma_x^2/\sigma_{\mathrm{e}}^2$ that can be understood as local signal-to-noise ratio (SNR) within the given DEM patch. High SNR patches with $\sigma_x^2/\sigma_{\mathrm{e}}^2 > 2$ are called texture informative (TI). For other patches, Hurst exponent estimation is not reliable and is evaluated using the inverse distance interpolation method [62] based on reliable estimates $\hat{H}_q$ from TI patches. In this manner, the interpolated Hurst exponent values $\hat{H}_{q.\mathrm{interp}}$ are obtained for each patch. To characterize interpolation error, we sequentially exclude one TI patch and interpolate Hurst exponent value for this patch using remaining TI patches. The interpolation error SD $\bar{\sigma}_{H_{q.\mathrm{interp}}}$ is calculated as SD of difference $\hat{H}_{q.\mathrm{interp}} - \hat{H}_q$ for all TI patches.

Two estimators for the error variance σ_{e}^2 and spatial correlation width σ^2_{Corr} can now be defined in the following form:

$$\left[\hat{\sigma}_x^2, \hat{H}_q, \hat{\sigma}_{\mathrm{e}}^2\right] = \underset{\sigma_x^2\geq 0, 0<H_q<1, \sigma_{\mathrm{e}}^2\geq 0, \sigma^2_{\mathrm{Corr}}=\hat{\sigma}^2_{\mathrm{Corr}}}{\arg\min} \times\left[\ln L(\Delta\hat{\mathbf{Z}};\boldsymbol{\theta}) - \frac{(H_q - \hat{H}_{q.\mathrm{interp}})^2}{2\bar{\sigma}^2_{H_{q.\mathrm{interp}}}}\right] \tag{8}$$

$$\left[\hat{\sigma}_x^2, \hat{H}_q, \hat{\sigma}^2_{\mathrm{Corr}}\right] = \underset{\sigma_x^2\geq 0, 0<H_q<1, \sigma_{\mathrm{e}}^2=\hat{\sigma}_{\mathrm{e}}^2, \sigma^2_{\mathrm{Corr}}\geq 0}{\arg\min} \times\left[\ln L(\Delta\hat{\mathbf{Z}};\boldsymbol{\theta}) - \frac{(H_q - \hat{H}_{q.\mathrm{interp}})^2}{2\bar{\sigma}^2_{H_{q.\mathrm{interp}}}}\right]. \tag{9}$$

In (8) and (9), we have taken into account the prior on the Hurst exponent as the additional term in the optimized log-likelihood function. This prior has maximal effect for the very homogeneous patches with low SNR, for which reliable Hurst exponent estimation is impossible. The effect becomes less pronounced with SNR increase.

FIMs $\mathbf{I}_{(\sigma_x^2, H_q, \sigma_{\mathrm{e}}^2)}$ and $\mathbf{I}_{(\sigma_x^2, H_q, \sigma^2_{\mathrm{Corr}})}$ for the estimators (8) and (9), respectively, are obtained from general matrix $\mathbf{I}_{\boldsymbol{\theta}}$ by eliminating row and column corresponding to the missing parameter and adding prior information on H_q by substituting $I_{H_qH_q}$ component with $I_{H_qH_q} + \bar{\sigma}^{-2}_{H_{q.\mathrm{interp}}}$.

CRLBs on σ_{e}^2 and σ^2_{Corr} estimate error are obtained by inverting $\mathbf{I}_{(\sigma_x^2, H_q, \sigma_{\mathrm{e}}^2)}$ and $\mathbf{I}_{(\sigma_x^2, H_q, \sigma^2_{\mathrm{Corr}})}$. The last elements of these matrices, $\sigma^2_{\sigma^2_{\mathrm{e}}}$ and $\sigma^2_{\sigma^2_{\mathrm{Corr}}}$, are CRLBs on σ_{e}^2 and σ^2_{Corr} estimate errors, respectively.

Taking into account error-free DEM and error independence between patches, estimators for the group of N_{group} patches can be straightforwardly formulated using (8) and (9)

$$\left[\hat{\mathbf{D}}_x, \hat{\mathbf{H}}_q, \hat{\sigma}_{\mathrm{e}}^2\right] = \underset{\mathbf{D}_x\geq 0, 0<\mathbf{H}_q<1, \sigma_{\mathrm{e}}^2\geq 0, \sigma^2_{\mathrm{Corr}}=\hat{\sigma}^2_{\mathrm{Corr}}}{\arg\min} \times\left[\sum_{v=1}^{N_{\mathrm{group}}}\left(\ln L(\Delta\hat{\mathbf{Z}}_v;\boldsymbol{\theta}_v) - \frac{(H_{q.v} - \hat{H}_{q.\mathrm{interp}.v})^2}{2\bar{\sigma}^2_{H_{q.\mathrm{interp}}}}\right)\right] \tag{10}$$

$$\left[\hat{\mathbf{D}}_x, \hat{\mathbf{H}}_q, \hat{\sigma}^2_{\text{Corr}}\right] = \underset{\mathbf{D}_x \geq 0, 0 < \mathbf{H}_q < 1, \sigma^2_{\text{e}} = \hat{\sigma}^2_{\text{e}}, \sigma^2_{\text{Corr}} \geq 0}{\arg\min} \times \left[\sum_{\upsilon=1}^{N_{\text{group}}} \left(\ln L(\Delta\hat{\mathbf{Z}}_\upsilon; \boldsymbol{\theta}_\upsilon) - \frac{(H_{q.\upsilon} - \hat{H}_{q.\text{interp}.\upsilon})^2}{2\bar{\sigma}^2_{H_{q.\text{interp}}}} \right) \right] \tag{11}$$

where $\Delta\hat{\mathbf{Z}}_\upsilon$ is the sample for υth patch, $\boldsymbol{\theta}_\upsilon = (\sigma^2_{x.\upsilon}, H_{q.\upsilon}, \sigma^2_{\text{e}}, \sigma^2_{\text{Corr}})$, $\sigma^2_{x.\upsilon}$, $H_{q.\upsilon}$, and $\hat{H}_{q.\text{interp}.\upsilon}$ are σ^2_x, H_q, and $\hat{H}_{q.\text{interp}}$ for υth patch, $\mathbf{D}_x = (\sigma^2_{x.1}, \sigma^2_{x.\upsilon}, \ldots, \sigma^2_{x.N_{\text{gr}}})$, and $\mathbf{H}_q = (H_{q.1}, H_{q.2}, \ldots, H_{q.N_{\text{gr}}})$. Note that the same error parameters are assumed for all patches in the group.

For nonoverlapping patches, error parameter estimates are independent. Therefore, CRLBs on σ^2_{e} and σ^2_{Corr} using a group of patches are given by $\sigma^2_{\sigma^2_{\text{e}}} = 1/\sum_{\upsilon=1}^{N_{\text{group}}} (\sigma^{-2}_{\sigma^2_{\text{e}.\upsilon}})$ and $\sigma^2_{\sigma^2_{\text{Corr}}} = 1/\sum_{\upsilon=1}^{N_{\text{group}}} (\sigma^{-2}_{\sigma^2_{\text{Corr}.\upsilon}})$, respectively.

Let us provide $\mathbf{R}_{\Delta\hat{\mathbf{Z}}}$ derivatives with respect to θ_i, $i = 1, \ldots, 4$

$$\frac{\partial \mathbf{R}_{\Delta\hat{\mathbf{Z}}}(k_1, k_2)}{\partial \sigma^2_x} = \sigma_x^{-2} R_{\Delta\mathbf{Z}}(t_{k_1}, s_{k_1}, t_{k_2}, s_{k_2}) \tag{12}$$

$$\frac{\partial \mathbf{R}_{\Delta\hat{\mathbf{Z}}}(k_1, k_2)}{\partial H_q} = 0.5\sigma_x^2 \big(\log\left(t^2_{k_1} + s^2_{k_1}\right)\left(t^2_{k_1} + s^2_{k_1}\right)^{H_q} + \log\left(t^2_{k_2} + s^2_{k_2}\right)\left(t^2_{k_2} + s^2_{k_2}\right)^{H_q} - \log((t_{k_1} - t_{k_2})^2 + (s_{k_1} - s_{k_2})^2) \times ((t_{k_1} - t_{k_2})^2 + (s_{k_1} - s_{k_2})^2)^{H_q}\big) \tag{13}$$

$$\frac{\partial \mathbf{R}_{\Delta\hat{\mathbf{Z}}}(k_1, k_2)}{\partial \sigma^2_{\text{e}}} = \begin{pmatrix} 1 + \exp\left(-\dfrac{d_0^2}{2\sigma^2_{\text{Corr}}}\right) \\ -\exp\left(-\dfrac{d_1^2}{2\sigma^2_{\text{Corr}}}\right) - \exp\left(-\dfrac{d_2^2}{2\sigma^2_{\text{Corr}}}\right) \end{pmatrix} \tag{14}$$

$$\frac{\partial \mathbf{R}_{\Delta\hat{\mathbf{Z}}}(k_1, k_2)}{\partial \sigma^2_{\text{Corr}}} = \frac{\sigma^2_{\text{e}}}{2\sigma^4_{\text{Corr}}} \begin{pmatrix} d_0^2 \exp\left(-\dfrac{d_0^2}{2\sigma^2_{\text{Corr}}}\right) \\ -d_1^2 \exp\left(-\dfrac{d_1^2}{2\sigma^2_{\text{Corr}}}\right) - d_2^2 \exp\left(-\dfrac{d_2^2}{2\sigma^2_{\text{Corr}}}\right) \end{pmatrix} \tag{15}$$

where $d_0 = ((t_{k_1} - t_{k_2})^2 + (s_{k_1} - s_{k_2})^2)^{1/2}$ and $d_1 = (t^2_{k_1} + s^2_{k_1})^{1/2}$, $d_2 = (t^2_{k_2} + s^2_{k_2})^{1/2}$.

Finally, DEM measurement error parameters estimation algorithm is detailed in Algorithm 1.

Algorithm 1 Estimation of DEM Measurement Error Parameters

Input: A number of a raster DEM tiles;

Output: DEM context-dependent error parameters (error variance σ^2_{e} and spatial correlation width σ^2_{Corr} dependence on predictor vector);

1. Split DEM tiles into non-overlapping patches; Reject unreliable patches (as described in subsection 5.1);
2. Set iteration number $k = 1$;
3. For each of N_{pt} selected patches, calculate predictor vector (e.g. stacking number, elevation) $\mathbf{p}_i$, $i = 1 \ldots N_{\text{pt}}$;
4. For each patch, calculate fBm field parameters vector according to (7). Interpolate Hurst exponent for low SNR patches (NI) using high SNR patches (TI);
5. For each patch, calculate Cramer-Rao lower bounds on σ^2_{e} or σ^2_{Corr} estimate error using (12) - (15); Calculate patch homogeneity index;
6. Group patches into NI groups using homogeneity index (as described in subsection 4.1); For each NI group calculate mean value of predictor vector $\bar{\mathbf{p}}_j$, $j = 1 \ldots N_{\text{NI}}$, N_{NI} is number of NI groups;
7. For each NI group, estimate error parameter s_j using (10) or (11);
8. Apply robust heteroscedastic regression to $(\bar{\mathbf{p}}_j, s_j)$ pairs to refine DEM context-dependent error parameter vector:$\boldsymbol{\theta}_{e.k}$ or $\boldsymbol{\theta}_{\text{Corr}.k}$;
9. Repeat 4-8 for both error variance σ^2_{e} and spatial correlation width σ^2_{Corr};
10. Increase iteration number: $k = k + 1$;
11. Repeat the steps from 4 to 10 till convergence defined as $||\boldsymbol{\theta}_{e.k} - \boldsymbol{\theta}_{e.k-1}|| < \varepsilon$ and $||\boldsymbol{\theta}_{\text{Corr}.k} - \boldsymbol{\theta}_{\text{Corr}.k-1}|| < \varepsilon$, where ε is small constant;

V. Application of Adapted mvcNI+fBm Estimator to Real DEMs Error Analysis

In this section, we apply the proposed mvcNI+fBm method to two global DEMs with 1 arc second (30 m at equator) spatial resolution: GDEM2 and AW3D30. More attention is paid to GDEM2 as it reveals the most complex measurement error behavior. To prove the mvcNI+fBm scalability, we test it on a sample granule of AW3D DEM with a 5-m spatial resolution. In addition, radar DEM TanDEM-X-DEM is analyzed to compare mvcNI+fBm results with theoretically predicted random noise SD. The obtained results for each DEM are compared with respective DEM accuracy analysis available in the literature.

A. Experimental Settings

For GDEM2 and AW3D30 DEMs, 59 tiles were used to estimate σ^2_{e} and σ^2_{Corr} model coefficients with the following lower left (southwest) corner pixels: N27–28E086–087, N30–32E035, N33–35E076, N47–48W001–002, N48–49E001–003, N48–49E031–032, N49–50E036–037, N50E099, N50E103, N51–52E099, N52E101–102, N53E103, and S23–28W067–070. Here, hyphen defines range of tiles with respect to latitude, longitude, or both; N and S denote the north and south latitudes, respectively; W and E denote the west and east longitudes, respectively.

Each tile has fixed latitudinal and longitudinal spatial resolution of 1 arc second (approximately 30 m at the equator) but expressed in meters, and resolution with respect to image rows and columns differs. To compensate for this effect, tiles

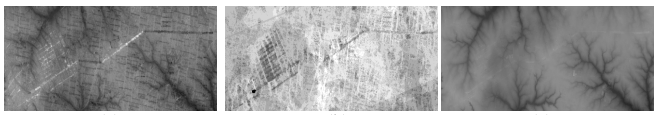

(a) (b) (c)

Fig. 5. Illustration of GDEM2 gross errors related to the stacking procedure. (a) GDEM2 patch, (b) GDEM2 stacking number, and (c) AW3D30 patch. Black corresponds to the elevation of 65 m and $N_{\text{stk}} = 0$, and white corresponds to 290 m and $N_{\text{stk}} = 11$.

were resampled to coarser 90-m resolution cell with respect to both spatial coordinates. For each tile, 10 000 nonoverlapping patches of 11×11 pixels were selected on a regular grid. The selected size of the patch is an experimentally found compromise between accuracy of error parameters estimates (that increase with patch size) and DEM patch homogeneity (that decreases with patch size). The stacking number for each pixel of these patches was obtained using quality assessment (QA) files supplied for each tile (the QA file has the same number of rows and columns as DEM tile with each pixel representing the corresponding N_{stk} value. QA file has extension.num for GDEM2 and suffix "STK" for AW3D). QA files were also interpolated to 90-m grid to match DEM tiles.

We set two criteria to decide whether a patch is reliable for measurement error parameter estimation: 1) it contains data provided by the "normal" workflow for the particular DEM and 2) patch is not significantly affected by GDEM2 stacking procedure artifacts (see the next paragraph). The first criterion for photogrammetric DEM excludes pixels where disparity measurement procedure fails, primary from lack of data (e.g., caused by clouds), water body (that are typically masked out), and low correlation areas (e.g., deserts). Those pixels are substituted from different sources (e.g., other DEMs) or remain as voids and do not characterize measurement error. Such pixels can be identified by a negative stacking number for GDEM2 and from mask information file (marked by "MSK" suffix) for AW3D, and from water indication mask ("WAM") files of Tan-DEM-X DEM.

The second criterion is for handling another problem causing gross elevation error is related to GDEM2 stacking procedure: it produces false elevation discontinuities if stacking number changes severely. This problem is illustrated in Fig. 5, where a GDEM2 DEM patch, the corresponding stacking number map, and the AW3D30 patch from the same location are shown. The false elevation discontinuity correlated with the stacking number discontinuity is clearly visible, while at AW3D30 patch, this feature is missing. To avoid this source of gross errors, the minimum $N_{\text{stk.min}}$ and maximum $N_{\text{stk.max}}$ numbers of stereo pairs were calculated for each patch. The patch was rejected if $N_{\text{stk.max}}/N_{\text{stk.min}} > 2$, thus limiting stacking number variability. All patches that were found reliable are further processed by the mvcNI+fBm estimator.

Predictor weights were set as $w_1 = 1$ and $w_2 = 0.01$ m^{-1} for N_{stk} and Z, respectively. Required homogeneity index for NI groups was experimentally set to 0.125. We found that in all cases, mvcNI+fBm converged in less than 15 iterations. Computational complexity of mvcNI+fBm is moderate: single iteration of mvcNI+fBm for 59 tiles takes about 5 h on Intel Core i5-7200U CPU. The algorithm can be significantly sped up by parallel processing of groups of fragments on GPU.

We use classical tools of linear regression to characterize regression models: generalized determination coefficient, partial residual plot, and significance test for predictor values using t-statistic [63], [64]. The generalized determination coefficient [65]: $R^2 = 1 - \exp(-(2/N_{\text{NI}})(l_R - l_U))$, where l_R is the log-likelihood for regression model restricted only with intercept, l_u is the log-likelihood of the unrestricted regression model, and N_{NI} is the number of estimates (number of NI groups). Assuming normal distribution of error parameter estimate errors provided by the mvcNI+fBm and omitting constants shared by both l_R and l_u, the log-likelihoods for restricted and unrestricted models take the following quite simple form: $l_R = -(1/2)\sum_{i=1}^{N_{\text{NI}}}((\hat{s}_i - s_{\text{const}})^2/\sigma_{s_i}^2)$ and $l_u = -(1/2)\sum_{i=1}^{N_{\text{NI}}}((\hat{s}_i - s_{\text{pr.i}})^2/\sigma_{s_i}^2)$, where $s_{\text{pr.i}}$ is the parameter prediction for ith measurement.

B. ASTER GDEM2 Experiment

The ASTER global DEM version 2 was released by the National Aeronautic and Space Administration (NASA), Washington, DC, USA, and the Ministry of Economy, Trade, and Industry (METI) of Japan in 2011 [23], [24]. Experimental assessment of the GDEM2 has been published in numerous articles including [22], [23], [66] among others.

The ASTER GDEM2 was produced from data collected by the ASTER sensor on board of the NASA Terra spacecraft, which is capable of collecting in-track stereo pairs using nadir- and aft-looking near-infrared cameras [67], [68]. The procedure for the GDEM2 generation is described in [58]. According to this procedure, elevation estimates are obtained via correlation-based registration with 5×5 pixel window. Curve fitting approach [69] is used to reach the subpixel registration accuracy. The search is performed in the along-track direction neglecting a small cross-track shift component appearing due to the contribution of earth rotation effects during the stereoscopic observation period. Multiple stereo pairs (stacking number up to 50) are used to obtain elevation estimates for a given area.

1) Measurement Error Variance Analysis: The results obtained for error parameter σ_{e}^2 are presented in Table I. It was found that models with quadratic dependence on elevation are more significant according to R^2 coefficient (R^2 is 0.4335 and 0.6298 for models $1 + Z$ and $1 + Z^2$; 0.7717 and 0.8954 for models $1 + N_{\text{stk}}^{-1} + Z + ZN_{\text{stk}}^{-1}$ and $1 + N_{\text{stk}}^{-1} + Z^2 + Z^2N_{\text{stk}}^{-1}$, respectively). Using only N_{stk} predictor, we get a low determination coefficient $R^2 = 0.1221$ (model $1 + N_{\text{stk}}^{-1}$). The second Z predictor notably increases R^2 to 0.6298 (model $1 + Z^2$). Using all terms in the model (4) increases R^2 even further to the value of 0.8954. Therefore, the influence of both predictors on σ_{e}^2 is significant. The estimated model for the GDEM2 elevation measurement error variance is given as follows:

$$\sigma_{\text{e}}^2 = 1.0293\ \text{m}^2 + 25.6667\ \text{m}^2 N_{\text{stk}}^{-1} + 4.8991 \cdot 10^{-7} Z^2 + 6.1069 \cdot 10^{-6} Z^2 N_{\text{stk}}^{-1}. \quad (16)$$

The partial residual plots for components of the model (16) with the highest R^2 (Fig. 6) reveal significance of

TABLE I

RESULTS OF THE ELEVATION MEASUREMENT ERROR PARAMETER ESTIMATION OBTAINED WITH THE mvcNI+fBm FOR THE ASTER GDEM2

Model type	R^2	Parameters	Parameter SDs	t-stats
Measurement noise variance				
$1+N_{\text{stk}}^{-1}+Z^2+Z^2N_{\text{stk}}^{-1}$	0.8954	$\sigma^2_{\text{Var01}} = 1.0293\ \text{m}^2$	$0.0648\ \text{m}^2$	15.8765
		$\sigma^2_{\text{Var02}} = 25.6637\ \text{m}^2$	$0.9898\ \text{m}^2$	25.9296
		$c_{\text{VarZ1}} = 4.8991\cdot10^{-7}$	$1.6400\cdot10^{-8}$	29.8722
		$c_{\text{VarZ2}} = 6.1069\cdot10^{-6}$	$2.6929\cdot10^{-7}$	22.6777
Measurement error correlation width (in 90 m pixels, Gaussian model)				
$1+Z^2$	0.8977	$\sigma^2_{\text{Corr01}} = 0.1937$	0.0023	83.0768
		$c_{\text{CorrZ1}} = 1.7786\cdot10^{-8}$	2.3397·10-10	76.0193

In total, 5331 $\hat{\sigma}^2_e$ estimates and 8044 $\hat{\sigma}^2_{\text{Corr}}$ estimates were obtained by the mvcNI+fBm. They cover predictor variation intervals from 3 to 49 for N_{stk} and from -400 to about 5500 m for Z. The percentage of detected outliers is about 0.1% for the error variance and about 7.5% for error correlation width.

each component. Note the practical absence of outliers among mvcNI+fBm estimates (outliers percentage is about 0.1% for σ^2_{e}).

Let us validate further the selected model (16) both qualitatively and quantitatively in comparison with GDEM2 analysis results provided in the available literature. For the ASTER instrument, $B = 0.6$ and $r = 15$ m. The ratio $(r/B) = 15$ m/pixel is conversion ratio between pixel and meter units. It is systematically used in the analysis below where conversion between measurement units is involved.

The value of σ_{e} at the sea level ($Z = 0$) and for one stereopair ($N_{\text{stk}} = 1$) is given as $(\sigma^2_{\text{Var01}} + \sigma^2_{\text{Var02}})^{1/2} = 5.1668$ m. This value was estimated by Fujisada *et al.* [58] (see [58, Fig. 10], kernel size 5×5 pixels) to vary from 0.2 to 0.3 pixels or, equivalently, from 5 to 7.5 m, depending on the terrain. One can conclude and underline good agreement between these two estimates.

The value of σ_{e} introduced in this article corresponds to the SD of elevation bias in [22]. Therefore, we can directly compare model (16) with the results by Becek [22]. The reported results of the dependence of SD of bias on N_{stk} make this comparison even more informative. The majority of 96 runways considered in [22] are situated at low altitudes near the sea level with the mean elevation of 234.7 m. We simplify model (16) by substituting $Z = 234.7$ m getting the reduced model $\sigma^2_{\text{e}} = 1.0563 + 26.0031N^{-1}_{\text{stk}}$. The results obtained with the reduced model were compared to those shown in [21, Fig. 10]. Both estimates are shown in Fig. 7 for N_{stk} varying from 0 to 50.

The results of the mvcNI+fBm and runway methods are highly consistent for $N_{\text{stk}} > 20$. For $N_{\text{stk}} < 20$, σ^2_{e} estimates obtained by the mvcNI+fBm are up to two times smaller than those provided by the runway method. The possible reason of this difference is the better robustness of mvcNI+fBm to gross GDEM2 errors and outliers that affect the GDEM2 for low stacking numbers as indicated by Becek [22].

The estimates of c_{VarZ1} and c_{VarZ2} related to epipolar line error show very significant influence of elevation on σ^2_{e}: σ_{e} at $Z = 6000$ m increases by 1.9…3.4 times as compared to this value at $Z = 0$ m making elevation influence the predominant error source at high elevations. The epipolar line error SD is measured in [58] to be about 0.15 pixels or 3.75 m for elevation about 4000 m (Mount Elbert). According to model (16), σ^2_{e} at elevation $Z = 4000$ m and typical number of stereo pairs $N_{\text{stk}} = 10$ increase by $4.899 \cdot 10^{-7}(4000\ \text{m})^2 + 6.107 \cdot 10^{-6}(4000\ \text{m})^2/10 = 17.61\ \text{m}^2$. This additional SD of $(17.61\ \text{m}^2)^{1/2} = 4.2$ m is very close to the value reported in [58].

2) Measurement Error Correlation Width Analysis: For the correlation width parameter (Table I), significant dependence on elevation can be observed (determination coefficient is about 0.85–0.9 for the models $1 + Z$ and $1 + Z^2$) revealing epipolar line error influence on measurement error correlation function. Similar to what occurs for modeling σ^2_{e}, models depending on Z are less relevant than models depending on Z^2 for modeling σ^2_{Corr}. Joint usage of two predictors, N_{stk} and Z, cannot definitely confirm or discard hypothesis of N_{stk} influence on correlation width: t-stats for terms dependent on N_{stk} have rather small values (less than 10; see partial regression plots in Fig. 6). Therefore, we consider model $1 + Z^2$ as the most relevant one for the GDEM2 measurement error spatial correlation width (numeric values are in 90-m pixels)

$$\sigma^2_{\text{Corr}} = 0.1937 + 1.7786 \cdot 10^{-8} Z^2. \tag{17}$$

The constant term of correlation width estimate obtained by the mvcNI+fBm method for $Z = 0$ is about 0.44 pixels at the resolution of 90 m that corresponds to 2.64 pixels at the ASTER resolution of 15 m. This value is about the half-size of 5×5 pixels correlation window, what is reasonable. For $Z = 5000$ m, correlation width increases almost twice to $\sigma_{\text{Corr}} = 0.8$ or 4.8 ASTER pixels. The value of correlation width estimate close to the correlation window size indicates that the measurement error correlation function shape could deviate from Gaussian one at least for high elevation values. Additional research is needed to clarify this hypothesis.

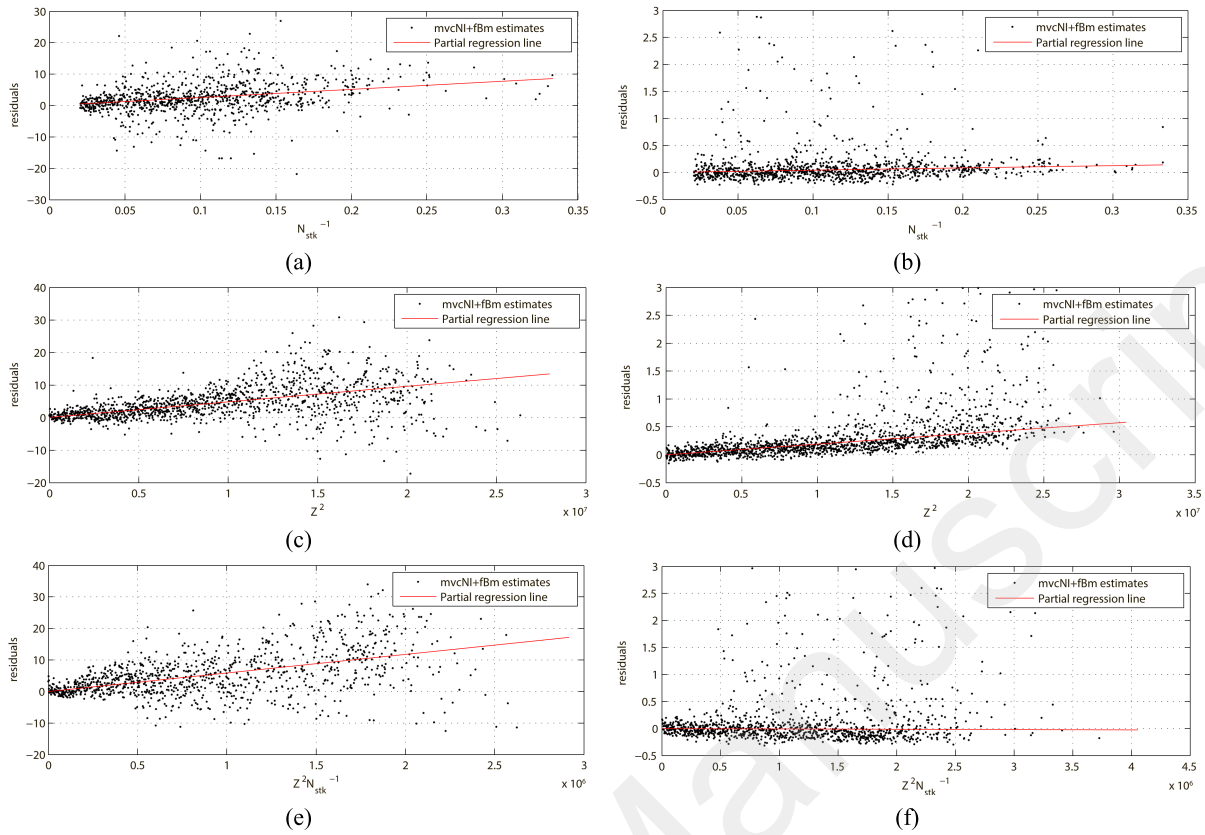

Fig. 6. Partial regression plots for (a), (c), and (e) σ_e^2 and (b), (d), and (f) σ_{Corr}^2 model coefficients.

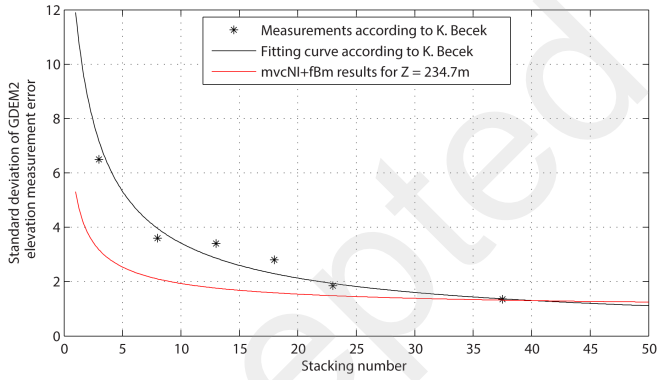

Fig. 7. Comparison of the mvNI+fBm results for the GDEM2 with the results obtained by Becek [22].

C. ALOS Experiment (5-m Resolution)

AW3D is a recent global DEM that is derived from the data generated by Panchromatic Remote-sensing Instrument for Stereo Mapping (PRISM), one of the onboard sensors carried in the ALOS. It has a high spatial resolution of 0.15 arc second (approximately 5 m at equator) and target vertical accuracy of 5 m (RMSE). The low-resolution version (30-m spacing) is generated by averaging the original one [70] and is provided free of charge. Elevation is estimated by correlation coefficient maximization according to the triplet image matching algorithm with correlation window size optimization [71]. For the PRISM instrument, $B = 0.5$ (between nadir and forward/aft-looking sensors) and $r = 2.5$ m. The ratio $(r/B) = 5$ m/pixel is conversion ratio between pixel and meter units.

Sample AW3D tile for the area of Yushan mountain, Taiwan, (central coordinates are 23°28′08.4″ N 120°57′36.0″ E, 4336 × 4702 pixels) were kindly provided by NTT DATA. As for the GDEM2, the AW3D tile was downscaled three times to a 15-m spatial resolution. For the AW3D, experiments do not reveal significance of elevation predictor on measurement error parameters (both σ_e^2 and σ_{Corr}^2, see Table II). This result indicates negligible epipolar line error for AW3D that can be related to higher accuracy of ALOS satellite ephemeris data [60] as compared to Terra satellite [58]. Similar to GDEM2, measurement error variance is strongly dependent on stacking number. Restricted amount of data available covers only the limited range of N_{stk} change from about 4 to 7. Therefore, σ_e^2 for infinite number of N_{stk} cannot be estimated with high precision. Surprisingly, σ_e^2 for AW3D and GDEM2 for sea level elevation is of the same order: σ_e is about 5 m for $N_{stk} = 1$. Converted to disparity error in sensor pixels, 5-m SD corresponds to about 0.2 pixels for GDEM2 [5 m/25(m/pixel)] and 1 pixel for AW3D [5 m/5(m/pixel)]. Such an elevated error SD may be related to peculiarities of stereo-matching algorithm implementation for AW3D. Measurement error correlation width for the AW3D is about 0.39 pixels at the resolution of 15 m.

TABLE II

RESULTS OF THE ELEVATION MEASUREMENT ERROR PARAMETER ESTIMATION OBTAINED WITH THE mvcNI+fBm FOR THE ALOS 3D WORLD, 5 m

Model type	R^2	Parameters	Parameter SDs	t-stats
Measurement error variance				
$1+N_{\text{stk}}^{-1}$	0.27306	$\sigma^2_{\text{Var01}} = 0.3558$ m^2	0.1441 m^2	2.4680
		$\sigma^2_{\text{Var02}} = 24.2965$ m^2	0.7402 m^2	32.8237
Measurement error correlation width (in 15 m pixels, Gaussian model)				
1	-//-	$\sigma^2_{\text{Corr01}} = 0.1525$	0.00227	67.0331
In total, 3337 $\hat{\sigma}_e^2$ estimates and 452 $\hat{\sigma}^2_{\text{Corr}}$ estimates were obtained by the mvcNI+fBm. They cover predictor variation intervals from 4 to 7 for N_{stk} and from 1000 to about 3800 m for Z. No outliers were detected for both error variance and correlation width.				

TABLE III

RESULTS OF THE ELEVATION MEASUREMENT ERROR PARAMETER ESTIMATION OBTAINED WITH THE mvcNI+fBm FOR THE ALOS 3D WORLD, 30 m

Model type	R^2	Parameters	Parameter SDs	t-stats
Measurement error variance				
$1+N_{\text{stk}}^{-1}$	0.03179	$\sigma^2_{\text{Var01}} = 0.3340$ m^2	0.00407 m^2	82.0500
		$\sigma^2_{\text{Var02}} = 0.2770$ m^2	0.02404 m^2	11.5208
Measurement error correlation width (in 90 m pixels, Gaussian model)				
1	-//-	$\sigma^2_{\text{Corr01}} = 0.2556$	0.00139	183.6447
In total, 8126 $\hat{\sigma}_e^2$ estimates and 5645 $\hat{\sigma}^2_{\text{Corr}}$ estimates were obtained by the mvcNI+fBm. They cover predictor variation intervals from 3 to 14 for N_{stk} and from -400 to about 5000 m for Z. The percentage of detected outliers is about 0.3% for the error variance and about 1.8% for error correlation width.				

D. ALOS Experiment (30-m Resolution)

For the AW3D30 (Table III) as for AW3D, the experiments reveal the significance of stacking number predictors for σ_{e}^2. For σ^2_{Corr}, both predictors are not significant. Measurement error variance for the AW3D30 is lower than the one for the GDEM2 even in the best settings (large stacking number and sea level elevation): $\sigma_{\text{Var01}} = 0.6140$ m for the AW3D30 as compared to $\sigma_{\text{Var01}} = 1.0145$ m for GDEM2. Taking into account that the AW3D30 is obtained by averaging AW3D pixels by six times with respect to both coordinates, σ_{e} for the AW3D30 should be six times lower than for the AW3D. This is actually observed for $N_{\text{stk}} = 1$: $\sigma_{\text{e.AW3D}}(1)/6 \approx 0.83$ m as compared to $\sigma_{\text{e.AW3D30}}(1) \approx 0.78$ m. For large values of N_{stk}, measurement error SD for the AW3D30 is comparable to the quantization error. In this extreme case, the mvcNI+fBm might not reveal decay of σ_{e}^2 with stacking number. Measurement error correlation width for the AW3D30 is about 0.2556 pixels at the resolution of 90 m.

E. TanDEM-X-DEM Experiment (90-m Resolution)

In the next experiment, we apply the mvcNI+fBm to the open 90-m resolution version of TanDEM-X-DEM—DEM created by interferometric processing of data from the two twin SAR satellites TerraSAR-X and TanDEM-X [31]. The unique feature of TanDEM-X-DEM important for this study is that it contains estimates of the DEM random error SD called height error map (HEM). The HEM is derived by rigorous error propagation on the basis of TanDEM-X platform characteristics, interferometric coherence, and geometrical considerations [31], [72]. HEM is provided for each DEM tile as auxiliary files with "HEM" suffix and contains pixel-wise estimate of TanDEM-X-DEM random error SD. For TanDEM-X-DEM, random error is understood in the same manner as in this work: "random errors are high-frequency errors with low spatial correlation contributing to both the point-to-point relative vertical accuracy and the absolute vertical accuracy" [72]; therefore, we consider HEM as σ_{e} estimate.

Random error for a DEM generated by a radar platform is dependent on many factors. The goal of this experiment is not to analyze these factors, but to verify agreement of HEM and mvcNI+fBm estimates. For this, we consider regression model in the form $1 + \text{HEM}^2$

$$\sigma_{\text{e}}^2 = \sigma^2_{\text{Var01}} + c_{\text{VarHEM}}\text{HEM}^2. \tag{18}$$

Assuming HEM is a correct estimate of TanDEM-X-DEM random error SD and mvcNI+fBm provides accurate estimates of σ_{e}, one expects $\sigma_{\text{e}}^2 = \text{HEM}^2$ and coefficients of model (18) should be $\sigma^2_{\text{Var01}} = 0$ and $c_{\text{VarHEM}} = 1$.

For TanDEM-X-DEM, we used the same DEM tiles and the same experiments settings as for the ASTER GDEM2 experiment. The complexity of TanDEM-X-DEM analysis exceeds that of ASTER GDEM2 because random noise SD is two orders of magnitude lower. For the considered tiles, HEM varies from 0.018 (0.01% quantile) to 3.5 m (99.99% quantile) with the mode equal to 0.05 m as compared to $2 \ldots 6$ m for

TABLE IV
RESULTS OF THE ELEVATION MEASUREMENT ERROR PARAMETER ESTIMATION OBTAINED WITH THE mvcNI+fBm FOR THE TANDEM-X-DEM, 90 m

Model type	R^2	Parameters	Parameter SDs	t-stats
Measurement error variance				
$1+HEM^2$	0.999	$\sigma^2_{\text{Var01}} = 0.00518$ m^2; $c_{\text{Var}HEM} = 2.82$	$3.63\cdot10^{-4}$ m^2; 0.102	14.29; 27.73
Measurement error correlation width (in 90 m pixels, exponential model)				
1	-//-	$\sigma^2_{\text{Corr01}} = 0.152$	0.042	3.62

In total, 504 $\hat{\sigma}^2_e$ estimates and 20 $\hat{\sigma}^2_{\text{Corr}}$ estimates were obtained by the mvcNI+fBm. They cover predictor variation intervals from 0.0190 to 0.711 for *HEM* and from -400 to about 5000 m for Z. The percentage of detected outliers is about 20% for both error variance and correlation width.

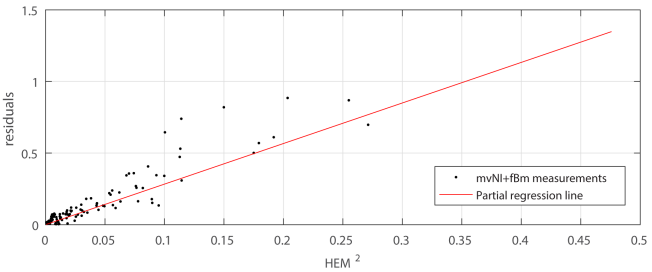

Fig. 8. Partial regression plots for σ^2_e model HEM component.

ASTER GDEM2. Measurement error estimation results are summarized in Table IV.

Both σ^2_{Var01} and c_{VarHEM} coefficients of the model (18) are significant. For values of HEM exceeding 0.2 m, $\hat{\sigma}_e$ estimated with the mvcNI+fBm is close to HEM and exceeds it by about 1.68 times. For HEM < 0.2, ratio between $\hat{\sigma}_e$ and HEM increases and reaches 2.2 for HEM equal 0.05. This result means that estimates provided by the mvcNI+fBm are close to theoretically predicted ones in the wide range of HEM. Discrepancy between the mvcNI+fBm estimates and HEM might be in part attributed to the fact that HEM is an optimistic estimate of TanDEM-X-DEM error; random noise with SD higher than HEM was reported in [73]. Significance of the HEM component is illustrated by the partial residual plots (Fig. 8).

VI. CONCLUSION

In this article, we have proposed and investigated application of the blind noise parameter estimator to characterize gridded DEM vertical error, specifically fine-scale elevation measurement error.

While BNPE is a well developed area, the new application scenario has not been covered by existing methods: the elevation measurement error SD is dependent on several predictors, while existing methods deal with signal-dependent noise model with only one predictor, namely, image intensity. Therefore, the recently proposed mvcNI+fBm estimator that is able to deal with multivariate noise signal-dependence has been modified and used to estimate both SD and spatial correlation width of DEM measurement error.

In Section V, the mvcNI+fBm has been applied to build bivariate models of ASTER GDEM2 and AW3D (both with 5- and 30-m spatial resolution) elevation measurement error. The two predictors in these models are the number of stereo pairs (responsible for stacking procedure influence) and elevation itself (responsible to epipolar line error influence). These models have been found consistent with the accuracy analysis results published in the available literature for GDEM2 and AW3D data. Not previously reported in the literature, our analysis reveals the epipolar line error as a very important factor responsible for the GDEM2 quality degradation for high elevations. The derived regression models for GDEM2, AW3D30, and AW3D can be used to predict elevation measurement error parameters for low relief areas (with elevation SD from 0 to about 15 m).

Experiment with TanDEM-X-DEM (90-m resolution) shows that estimates of the mvcNI+fBm closely follows theoretically predicted SD (HEM) provided by the German Aerospace Center (DLR). It is important to mention that the mvcNI+fBm was validated in very wide range of measurements error SD, from about 5 m for ASTER GDEM2 down to 0.05 m for TanDEM-X-DEM.

While the proposed no-reference approach to DEM accuracy analysis cannot provide information on DEM bias, the detailed study of DEM measurement error SD and correlation width can see variety of applications including the analysis of LiDAR or RADAR-derived raster DEMs, direct efficiency comparison of different approaches for stereo matching or interferometric phase reconstruction, and the analysis of sensor-related (e.g., jitter causing the epipolar line error of GDEM2) components in elevation measurement error. Future work is seen in the direction of using additional observable predictors (especially related to vegetation cover). Another direction is to overcome the inability of characterizing DEM error in high relief areas.

REFERENCES

[1] S. Voigt, T. Kemper, T. Riedlinger, R. Kiefl, K. Scholte, and H. Mehl, "Satellite image analysis for disaster and crisis-management support," *IEEE Trans. Geosci. Remote Sens.*, vol. 45, no. 6, pp. 1520–1528, Jun. 2007.

[2] H. Chaabouni-Chouayakh, P. D'Angelo, T. Krauss, and P. Reinartz, "Automatic urban area monitoring using digital surface models and shape features," in *Proc. Joint Urban Remote Sens. Event*, Apr. 2011, pp. 85–88.

[3] Y. Zhang, Y. Wan, X. Huang, and X. Ling, "DEM-assisted RFM block adjustment of pushbroom nadir viewing HRS imagery," *IEEE Trans. Geosci. Remote Sens.*, vol. 54, no. 2, pp. 1025–1034, Feb. 2016.

[4] A. Nelson, H. I. Reuter, and P. Gessler, "DEM production methods and sources," in *Developments in Soil Science*, vol. 33, T. Hengl and H. I. Reuter, Eds. Amsterdam, The Netherlands: Elsevier, 2009, ch. 3, pp. 65–85.

[5] C. Chen, Y. Li, N. Zhao, and C. Yan, "Robust interpolation of DEMs from LiDAR-derived elevation data," *IEEE Trans. Geosci. Remote Sens.*, vol. 56, no. 2, pp. 1059–1068, Feb. 2018.

[6] P. F. Fisher and N. J. Tate, "Causes and consequences of error in digital elevation models," *Prog. Phys. Geography*, vol. 30, pp. 467–489, Aug. 2006.

[7] K. W. Holmes, O. A. Chadwick, and P. C. Kyriakidis, "Error in a USGS 30-meter digital elevation model and its impact on terrain modeling," *J. Hydrol.*, vol. 233, nos. 1–4, pp. 154–173, Jun. 2000.

[8] M. F. Hutchinson, "Adding the Z-dimension," in *The Handbook of Geographic Information Science*. Oxford, U.K.: Blackwell, 2008, pp. 144–168.

[9] H. Papasaika, D. Poli, and E. Baltsavias, "Fusion of digital elevation models from various data sources," in *Proc. Int. Conf. Adv. Geographic Inf. Syst. Web Services*, Feb. 2009, pp. 117–122.

[10] H. Schultz, E. M. Riseman, F. R. Stolle, and W. Dong-Min, "Error detection and DEM fusion using self-consistency," in *Proc. 7th IEEE Int. Conf. Comput. Vis.*, vol. 2, Sep. 1999, pp. 1174–1181.

[11] L. Yue, H. Shen, L. Zhang, X. Zheng, F. Zhang, and Q. Yuan, "High-quality seamless DEM generation blending SRTM-1, ASTER GDEM v2 and ICESat/GLAS observations," *ISPRS J. Photogramm. Remote Sens.*, vol. 123, pp. 20–34, Jan. 2017.

[12] J. Takaku, A. Iwasaki, and T. Tadono, "Adaptive filter for improving quality of ALOS PRISM DSM," in *Proc. IEEE Int. Geosci. Remote Sens. Symp.*, Jul. 2016, pp. 5370–5373.

[13] M. Lebrun, M. Colom, A. Buades, and J. M. Morel, "Secrets of image denoising cuisine," *Acta Numerica*, vol. 21, no. 1, pp. 475–576, 2012.

[14] H. I. Reuter, T. Hengl, P. Gessler, and P. Soille, "Preparation of DEMs for geomorphometric analysis," in *Developments in Soil Science*, vol. 33, T. Hengl and H. I. Reuter, Eds. Amsterdam, The Netherlands: Elsevier, 2009, ch. 4, pp. 87–120.

[15] C. Chen, F. Liu, Y. Li, C. Yan, and G. Liu, "A robust interpolation method for constructing digital elevation models from remote sensing data," *Geomorphology*, vol. 268, pp. 275–287, Sep. 2016.

[16] A. J. A. M. Temme, G. B. M. Heuvelink, J. M. Schoorl, and L. Claessens, "Geostatistical simulation and error propagation in geomorphometry," in *Developments in Soil Science*, vol. 33, T. Hengl and H. I. Reuter, Eds. Amsterdam, The Netherlands: Elsevier, 2009, ch. 5, pp. 121–140.

[17] J. P. Wilson, "Digital terrain modeling," *Geomorphology*, vol. 137, no. 1, pp. 107–121, 2012.

[18] T. Tadono, M. Shimada, M. Watanabe, T. Hashimoto, and T. Iwata, "Calibration and validation of PRISM onboard ALOS," *Int. Arch. Photogramm., Remote Sens. Spatial Inf. Sci.*, vol. 35, no. 1, pp. 13–18, 2004.

[19] C. C. Carabajal and D. J. Harding, "SRTM C-band and ICESat laser altimetry elevation comparisons as a function of tree cover and relief," *Photogramm. Eng. Remote Sens.*, vol. 72, no. 3, pp. 287–298, Mar. 2006.

[20] T. Toutin, "Comparison of stereo-extracted DTM from different high-resolution sensors: SPOT-5, EROS-A, IKONOS-II, and QuickBird," *IEEE Trans. Geosci. Remote Sens.*, vol. 42, no. 10, pp. 2121–2129, Oct. 2004.

[21] L. Barreiro-Fernández, S. Buján, D. Miranda, U. Diéguez-Aranda, and E. González-Ferreiro, "Accuracy assessment of LiDAR-derived digital elevation models in a rural landscape with complex terrain," *J. Appl. Remote Sens.*, vol. 10, no. 1, Feb. 2016, Art. no. 016014.

[22] K. Becek, "Assessing global digital elevation models using the runway method: The advanced spaceborne thermal emission and reflection radiometer versus the shuttle radar topography mission case," *IEEE Trans. Geosci. Remote Sens.*, vol. 52, no. 8, pp. 4823–4831, Aug. 2014.

[23] T. Tachikawa, M. Hato, M. Kaku, and A. Iwasaki, "Characteristics of ASTER GDEM version 2," in *Proc. IEEE Int. Geosci. Remote Sens. Symp.*, Jul. 2011, pp. 3657–3660.

[24] H. Fujisada, M. Urai, and A. Iwasaki, "Technical methodology for ASTER global DEM," *IEEE Trans. Geosci. Remote Sens.*, vol. 50, no. 10, pp. 3725–3736, Oct. 2012.

[25] B. Rabus, M. Eineder, A. Roth, and R. Bamler, "The shuttle radar topography mission—A new class of digital elevation models acquired by spaceborne radar," *ISPRS J. Photogramm. Remote Sens.*, vol. 57, no. 4, pp. 241–262, Feb. 2003.

[26] B. Vozel *et al.*, "Blind determination of noise type for spaceborne and airborne remote sensing," in *Multivariate Image Processing*, C. Collet, J. Chanussot, K. Chehdi, Eds. Hoboken, NJ, USA: Wiley, 2010, p. 464.

[27] F. D. Van der Meer and S. M. De Jong, *Imaging Spectrometry: Basic Principles and Prospective Applications*, vol. 4. Dordrecht, The Netherlands: Kluwer, 2011.

[28] M. Uss, B. Vozel, V. Lukin, and K. Chehdi, "Analysis of signal-dependent sensor noise on JPEG 2000-compressed Sentinel-2 multi-spectral images," *Proc. SPIE*, vol. 10427, Oct. 2017, Art. no. 104270Y.

[29] *NTT DATA and RESTEC Distribute AW3Dtm Digital 3D Topographic Data*. Accessed: Nov. 12, 2019. [Online]. Available: http://aw3d.jp/en/

[30] ALOS Global Digital Surface Model, AW3D30. *ALOS World 3D-30m*. Accessed: Nov. 12, 2019. [Online]. Available: http://www.eorc.jaxa.jp/ALOS/en/aw3d30/

[31] P. Rizzoli *et al.*, "Generation and performance assessment of the global TanDEM-X digital elevation model," *ISPRS J. Photogramm. Remote Sens.*, vol. 132, pp. 119–139, Oct. 2017.

[32] A. Shortridge and J. Messina, "Spatial structure and landscape associations of SRTM error," *Remote Sens. Environ.*, vol. 115, no. 6, pp. 1576–1587, Jun. 2011.

[33] H. Liu and K. C. Jezek, "Investigating DEM error patterns by directional variograms and Fourier analysis," *Geographical Anal.*, vol. 31, no. 3, pp. 249–266, 1999.

[34] W. J. Burns, J. A. Coe, B. S. Kaya, and L. Ma, "Analysis of elevation changes detected from multi-temporal LiDAR surveys in forested landslide terrain in western Oregon," *Environ. Eng. Geosci.*, vol. 16, no. 4, pp. 315–341, 2010.

[35] J. Müller, I. Gärtner-Roer, P. Thee, and C. Ginzler, "Accuracy assessment of airborne photogrammetrically derived high-resolution digital elevation models in a high mountain environment," *ISPRS J. Photogramm. Remote Sens.*, vol. 98, pp. 58–69, Dec. 2014.

[36] K. Becek, "Investigating error structure of shuttle radar topography mission elevation data product," *Geophys. Res. Lett.*, vol. 35, no. 15, pp. 1–5, Aug. 2008.

[37] D. Zoran and Y. Weiss, "Scale invariance and noise in natural images," in *Proc. IEEE 12th Int. Conf. Comput. Vis.*, Sep./Oct. 2009, pp. 2209–2216.

[38] C. Liu, R. Szeliski, S. B. Kang, C. L. Zitnick, and W. T. Freeman, "Automatic estimation and removal of noise from a single image," *IEEE Trans. Pattern Anal. Mach. Intell.*, vol. 30, no. 2, pp. 299–314, Feb. 2008.

[39] M. L. Uss, B. Vozel, V. V. Lukin, and K. Chehdi, "Local signal-dependent noise variance estimation from hyperspectral textural images," *IEEE J. Sel. Topics Signal Process.*, vol. 5, no. 3, pp. 469–486, Jun. 2011.

[40] L. Alparone, M. Selva, B. Aiazzi, S. Baronti, F. Butera, and L. Chiarantini, "Signal-dependent noise modelling and estimation of new-generation imaging spectrometers," in *Proc. 1st Workshop Hyperspectral Image Signal Process., Evol. Remote Sens.*, Aug. 2009, pp. 1–4.

[41] B. Aiazzi, L. Alparone, S. Baronti, M. Selva, and L. Stefani, "Unsupervised estimation of signal-dependent CCD camera noise," *EURASIP J. Adv. Signal Process.*, vol. 2012, p. 231, Oct. 2012.

[42] S. K. Abramov, N. N. Ponomarenko, B. Vozel, and K. Chehdi, "Methods for blind evaluation of noise variance in multichannel optical and radar images," *Telecommun. Radio Eng.*, vol. 65, nos. 6–10, pp. 527–556, Jun. 2006.

[43] A. Foi, M. Trimeche, V. Katkovnik, and K. Egiazarian, "Practical Poissonian-Gaussian noise modeling and fitting for single-image raw-data," *IEEE Trans. Image Process.*, vol. 17, no. 10, pp. 1737–1754, Oct. 2008.

[44] L. Azzari and A. Foi, "Gaussian-Cauchy mixture modeling for robust signal-dependent noise estimation," in *Proc. IEEE Int. Conf. Acoust., Speech Signal Process.*, vol. 2014, pp. 5357–5361.

[45] M. L. Uss, B. Vozel, V. V. Lukin, and K. Chehdi, "Image informative maps for component-wise estimating parameters of signal-dependent noise," *J. Electron. Imag.*, vol. 22, no. 1, p. 013019, 2013.

[46] M. Colom, M. Lebrun, A. Buades, and J.-M. Morel, "Nonparametric multiscale blind estimation of intensity-frequency-dependent noise," *IEEE Trans. Image Process.*, vol. 24, no. 10, pp. 3162–3175, Oct. 2015.

[47] M. L. Uss, B. Vozel, V. V. Lukin, and K. Chehdi, "Maximum likelihood estimation of spatially correlated signal-dependent noise in hyperspectral images," *Opt. Eng.*, vol. 51, no. 11, 2012, Art. no. 111712.

[48] A. Danielyan and A. Foi, "Noise variance estimation in nonlocal transform domain," in *Proc. Int. Workshop Local Non-Local Approximation Image Process.*, Aug. 2009, pp. 41–45.

[49] T. Hengl and I. S. Evans, "Mathematical and digital models of the land surface," in *Developments in Soil Science*, vol. 33, T. Hengl and H. I. Reuter, Eds. Amsterdam, The Netherlands: Elsevier, 2009, ch. 2, pp. 31–63.

[50] K. Torlegård, A. Östman, and R. Lindgren, "A comparative test of photogrammetrically sampled digital elevation models," *Photogrammetria*, vol. 41, no. 1, pp. 1–16, Oct. 1986.

[51] Y. Tsin, V. Ramesh, and T. Kanade, "Statistical calibration of CCD imaging process," in *Proc. 8th IEEE Int. Conf. Comput. Vis.*, vol. 1, Jul. 2001, pp. 480–487.
[52] B. Aiazzi, L. Alparone, and S. Baronti, "A robust method for parameter estimation of signal-dependent noise models in digital images," in *Proc. 13th Int. Conf. Digit. Signal Process.*, vol. 2, Jul. 1997, pp. 601–604.
[53] B. Pesquet-Popescu and J. L. Vehel, "Stochastic fractal models for image processing," *IEEE Signal Process. Mag.*, vol. 19, no. 5, pp. 48–62, Sep. 2002.
[54] C. C. Barton, R. Paul, and L. Pointe, *Fractals in the Earth Sciences*. New York, NY, USA: Plenum Press, 1995.
[55] J. Feder, *Fractals*. Berlin, Germany: Springer, 2013.
[56] M. L. Uss, B. Vozel, V. A. Dushepa, V. A. Komjak, and K. Chehdi, "A precise lower bound on image subpixel registration accuracy," *IEEE Trans. Geosci. Remote Sens.*, vol. 52, no. 6, pp. 3333–3345, Jun. 2014.
[57] R. Hartley and A. Zisserman, *Multiple view geometry in computer vision*. Cambridge, U.K.: Cambridge Univ. Press, 2003.
[58] H. Fujisada, M. Urai, and A. Iwasaki, "Advanced methodology for ASTER DEM generation," *IEEE Trans. Geosci. Remote Sens.*, vol. 49, no. 12, pp. 5080–5091, Dec. 2011.
[59] X. Shen, P. Palmer, P. F. McLauchlan, and A. Hilton, "Error propogation from camera motion to epipolar constraint," in *Proc. BMVC*, 2000, pp. 1–10.
[60] T. Tadono, H. Ishida, F. Oda, S. Naito, K. Minakawa, and H. Iwamoto, "Precise global DEM generation by ALOS PRISM," *ISPRS Ann. Photogramm., Remote Sens. Spatial Inf. Sci.*, vol. 2, pp. 71–76, May 2014.
[61] S. M. Kay, *Fundamentals of Statistical Signal Processing: Estimation Theory*. London, U.K.: Prentice-Hall, 1993.
[62] D. Shepard, "A two-dimensional interpolation function for irregularly-spaced data," in *Proc. 23rd ACM Nat. Conf.*, Aug. 1968, pp. 517–524.
[63] G. A. Seber and A. J. Lee, *Linear Regression Analysis*, vol. 936. Hoboken, NJ, USA: Wiley, 2012.
[64] D. Altman, D. Machin, T. Bryant, and M. Gardner, *Statistics with Confidence: Confidence Intervals and Statistical Guidelines*. Hoboken, NJ, USA: Wiley, 2013.
[65] L. Magee, "R^2 measures based on wald and likelihood ratio joint significance tests," *Amer. Statistician*, vol. 44, no. 3, pp. 250–253, 1990.
[66] J. Goncalves and A. Oliveira, "Accuracy analysis of DEMs derived from ASTER imagery," *Int. Arch. Photogramm. Remote Sens.*, vol. 35, pp. 168–172, Jul. 2004.
[67] H. Fujisada, A. Iwasaki, and S. Hara, "ASTER stereo system performance," *Proc. SPIE*, vol. 4540, pp. 39–49, Dec. 2001.
[68] A. Iwasaki and H. Fujisada, "ASTER geometric performance," *IEEE Trans. Geosci. Remote Sens.*, vol. 43, no. 12, pp. 2700–2706, Dec. 2005.
[69] M. Debella-Gilo and A. Kääb, "Sub-pixel precision image matching for measuring surface displacements on mass movements using normalized cross-correlation," *Remote Sens. Environ.*, vol. 115, no. 1, pp. 130–142, Jan. 2011.
[70] J. Takaku, T. Tadono, and K. Tsutsui, "Generation of high resolution global DSM from ALOS PRISM," *Int. Arch. Photogramm., Remote Sens. Spatial Inf. Sci.*, vol. 40, pp. 243–248, May 2014.
[71] J. Takaku *et al.*, "High resolution DEM generation from ALOS PRISM data," in *Proc. IEEE Int. Geosci. Remote Sens. Symp.*, Jul. 2007, pp. 1974–1977.
[72] B. Wessel, *TanDEM-X Ground Segment–DEM Products Specification Document*, Public document TD-GS-PS-0021, 2013.
[73] P. Rizzoli, B. Bräutigam, T. Kraus, M. Martone, and G. Krieger, "Relative height error analysis of TanDEM-X elevation data," *ISPRS J. Photogramm. Remote Sens.*, vol. 73, pp. 30–38, Sep. 2012.

Mikhail L. Uss received the master's degree (Hons.) in radio engineering from the Kharkov Aviation Institute (now National Aerospace University), Kharkiv, Ukraine, in 2002, the Candidate of Technical Science degree in digital signal processing (DSP) for remote sensing from National Aerospace University in 2006, and the Ph.D. degree (Hons.) in signal processing and telecommunications from the University of Rennes 1, Lannion, France, in 2011.

From 2005 to 2015, he was with the Department of Aircraft Radioelectronic Systems Design, National Aerospace University, where he was also a Docent and the Head from 2012 to 2015, and is currently with the Department of Information-Communication Technologies. His research interests include remote sensing data processing, machine and deep learning, image registration, and blind estimation of image noise characteristics.

Benoit Vozel received the State Engineering degree, the M.Sc. degree in control and computer science, and the Ph.D. degree in applied sciences from the Ecole Centrale de Nantes, Nantes, France, in 1991 and 1994, respectively.

Since 1995, he has been with the Engineering School of Applied Sciences and Technology, University of Rennes 1, Lannion, France, where he is a currently a member of the SHINE (SAR and Hyperspectral Multimodal Imaging and Signal Processing, Electromagnetic Modeling) Team, Institute of Electronics and Telecommunications of Rennes (IETR CNRS UMR 6164). His research interests include the blind estimation of noise characteristics, blind image restoration, adaptive multichannel signal and image processing, and remote sensing data processing.

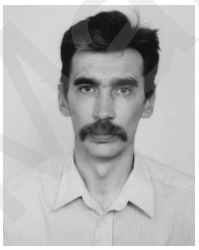

Vladimir V. Lukin received the master's degree (Hons.) in radio engineering from the Kharkov Aviation Institute (now National Aerospace University), Kharkiv, Ukraine, in 1983.

He presented the thesis of Candidate of Technical Science in 1988 and Doctor of Technical Science in 2002 in digital signal processing (DSP) for remote sensing. He is currently the Chairman and a Professor with the Department of Information-Communication Technologies, National Aerospace University. Since 1995, he has been in cooperation with the Tampere University of Technology, Tampere, Finland. His research interests include digital signal/image processing, remote sensing data processing, image filtering, and compression.

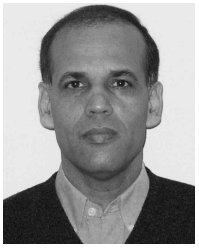

Kacem Chehdi received the Ph.D. and Habilitation à diriger des recherches degrees in signal processing and telecommunications from the University of Rennes 1, Lannion, France, in 1986 and 1992, respectively.

He has been a Professor of signal and image processing with the Engineering School of Applied Sciences and Technology, University of Rennes 1, since 1993, where he is a currently the Co-Head of the SHINE (SAR and Hyperspectral Multimodal Imaging and Signal Processing, Electromagnetic Modeling) Team, Institute of Electronics and Telecommunications of Rennes (IETR CNRS UMR 6164). His research interests include blind restoration and filtering, unsupervised classification, and adaptive decision-making systems.